Title
The effects of boundary topography on convection in Earth's core

Journal
Geophysical Journal International, 189(2)

ISSN
0956-540X

Authors
Calkins, Michael A
Noir, Jérôme
Eldredge, Jeff D
et al.

Publication Date
2012-05-01

DOI
10.1111/j.1365-246x.2012.05415.x

Peer reviewed

Geophysical Journal International

Geophys. J. Int. (2012) doi: 10.1111/j.1365-246X.2012.05415.x

The effects of boundary topography on convection in Earth's core

Michael A. Calkins,[1,2]★ Jérôme Noir,[3] Jeff D. Eldredge[1] and Jonathan M. Aurnou[2]

[1]*Department of Mechanical and Aerospace Engineering, University of California, Los Angeles,* CA 90095*, USA. E-mail: michael.calkins@colorado.edu*
[2]*Department of Earth and Space Sciences, University of California, Los Angeles,* CA 90095*, USA*
[3]*Institut für Geophysik, Swiss Federal Institute of Technology, Zurich, Switzerland*

Accepted 2012 February 8. Received 2012 January 29; in original form 2011 April 6

SUMMARY

We present the first investigation that explores the effects of an isolated topographic ridge on thermal convection in a planetary core-like geometry and using core-like fluid properties (i.e. using a liquid metal-like low Prandtl number fluid). The model's mean azimuthal flow resonates with the ridge and results in the excitation of a stationary topographic Rossby wave. This wave generates recirculating regions that remain fixed to the mantle reference frame. Associated with these regions is a strong longitudinally dependent heat flow along the inner core boundary; this effect may control the location of melting and solidification on the inner core boundary. Theoretical considerations and the results of our simulations suggest that the wavenumber of the resonant wave, L_R, scales as $Ro^{-1/2}$, where Ro is the Rossby number. This scaling indicates that small-scale flow structures [wavenumber $m \sim \mathcal{O}(10^2 - 10^3)$] in the core can be excited by a topographic feature on the core–mantle boundary. The effects of strong magnetic diffusion in the core must then be invoked to generate a stationary magnetic signature that is comparable to the scale of observed geomagnetic structures [$m \lesssim \mathcal{O}(10)$].

Key words: Numerical solutions; Dynamo: theories and simulations; Magnetic anomalies: modelling and interpretation; Core, outer core and inner core; Dynamics: convection currents, and mantle plumes; Planetary interiors.

1 INTRODUCTION

Observations of the geomagnetic field show the presence of high-latitude flux patches that have remained spatially fixed relative to the mantle for approximately 400 yr (e.g. Gubbins & Bloxham 1987). Palaeomagnetic studies have sought to construct a more reliable time-averaged geomagnetic field by extending records back as much as 5 Myr (Johnson & Constable 1997; Kelly & Gubbins 1997). Many workers employing palaeomagnetic data have found significant non-zonal structure in the time-averaged field (Gubbins & Kelly 1993; Johnson & Constable 1997; Kelly & Gubbins 1997; Korte & Constable 2006), although some have not (Carlut & Courtillot 1998).

Any non-zonal structure in the time-averaged geomagnetic field would likely imply that convective structures in the core interact with thermal, electromagnetic or topographic heterogeneities at the core–mantle boundary (CMB). In addition, lateral variations in the thermal conductivity of the mantle near the CMB can result in a heterogeneous heat flux across this interface. Much work has been devoted to understanding thermal core–mantle coupling (Bloxham & Gubbins 1987; Zhang & Gubbins 1993; Sumita & Olson 1999, 2002; Willis *et al.* 2007; Aubert *et al.* 2008; Davies *et al.* 2009). Topographic core–mantle coupling has been of interest for understanding the axial torques (Hide 1969; Anufriev & Braginsky 1975, 1977a,b; Moffatt 1978; Jault & Le Mouël 1989; Jault & Le Mouël 1990, 1991; Kuang & Bloxham 1993; Kuang & Chao 2001) and the equatorial torques (Hide *et al.* 1996; Hulot *et al.* 1996) that the fluid core exerts on the mantle. Comparatively fewer studies have examined the explicit role that CMB topography plays in altering the convective dynamics of the core (Bell & Soward 1996; Bassom & Soward 1996; Herrmann & Busse 1998; Westerburg & Busse 2003). Of these works, only a single numerical study (Herrmann & Busse 1998) and a related laboratory experiment (Westerburg & Busse 2003) have been carried out to examine the effects of CMB topography on the convective dynamics of the core. More work is necessary to determine the conditions under which CMB topography is important in the core, and whether these effects are likely to be manifested in the structure of the observed geomagnetic field.

Topographic and thermal heterogeneities on the CMB are the result of convection occurring in the overlying mantle. Mountains and ridges extending down into the core, for instance, can be formed by cold, downwelling material that comes to rest on the CMB. Similarly, hot plumes that detach from the CMB induce stresses in the mantle that may drag the CMB upward towards the Earth's surface. Numerical simulations of mantle convection demonstrate that these processes do occur at the CMB, though the details of the resulting CMB structure are dependent upon the local rheological properties of the mantle (Lassak *et al.* 2007; Yoshida 2008; Lassak *et al.* 2010).

★Now at: Department of Applied Mathematics, University of Colorado, Boulder, CO 80309, USA.

Seismic studies have investigated the shape of the CMB, though the results have been strongly model-dependent due largely to the presence of strongly heterogeneous material at the base of the mantle (Morelli & Dziewonski 1987; Doornbos & Hilton 1989; Rodgers & Wahr 1993; Sze & van der Hilst 2003). These investigations have reported topographic amplitudes as high as $\mathcal{O}(10)$ km. The recent work of Tanaka (2010) finds topographic amplitudes of up to ± 2 km, an estimate that we will use in this study.

The importance of topography on the dynamics of geometrically thin rotating fluid systems such as the Earth's atmosphere and ocean is well known and has motivated numerous studies (e.g. Maxworthy 1977; Charney & DeVore 1979; Legras & Ghil 1985; Wolff *et al.* 1991; Pfeffer *et al.* 1993; Weeks *et al.* 1997; Tian *et al.* 2001; Read & Risch 2011). Indeed, coupled with variations in temperature on the Earth's surface, the Himalaya and Rocky mountain ranges in the northern hemisphere represent one of the primary contributions to the time-averaged zonally asymmetric flow in the atmosphere that is characterized by a predominantly $m \approx 2$ wavenumber (Held *et al.* 2002). Laboratory experiments and numerical simulations of zonal flow interaction with topography have been successful at reproducing some of the observed large-scale structure in the atmosphere and ocean (Maxworthy 1977; Weeks *et al.* 1997; Tian *et al.* 2001; Read & Risch 2011). In contrast, very little is known about the dynamical effects of CMB topography on the convective dynamics of the core. Whereas the Rossby number (i.e. the ratio of inertia to Coriolis force) for the atmosphere is $\sim 10^{-1}$, in the core the Rossby number is closer to $\sim 10^{-6}$. This small value implies that the influence of the Coriolis force within the core is very strong, which suggests that CMB topography may influence the structure of core flow.

Core-related topographical studies have so far been limited to sinusoidal topography of a single wavelength and to low Reynolds numbers (i.e. the ratio of inertia to viscous forces) (Anufriev & Braginsky 1975, 1977a,b; Bassom & Soward 1996; Bell & Soward 1996; Herrmann & Busse 1998; Westerburg & Busse 2003). Bell & Soward (1996) examined the effects of topography in the annulus model of rapidly rotating convection (e.g. Busse 1970). They demonstrated that the buoyancy force can act directly on the geostrophic flow when topography is present, thus driving a mean flow at the onset of convective motions. Bassom & Soward (1996) extended the work of Bell & Soward (1996) to the case of a full sphere, showing that near the onset of convection topography induces a localized form of convection adjacent to the boundary. Herrmann & Busse (1998) also employed the annulus model to examine how the critical Rayleigh number changes with topographic amplitude and topographic wavenumber, and investigated the weakly non-linear properties of the resonant mode that is excited by the topography.

Further work is necessary to understand how the turbulent, high Reynolds number ($\sim 10^8$) flow of the core responds to CMB topography that contains a range of wavelengths. For this reason, this study focuses entirely on the interaction of chaotic non-magnetic flows with a single Gaussian topographic feature. Gaussian topography is useful because it is characterized by a broad range of wavelengths, and is therefore more likely to model realistic conditions at the CMB. This choice of topography also allows for resonance with any zonal flow that is produced in our simulations, provided viscous forces are sufficiently weak (e.g. Vallis 2006).

In the present work, we employ the 2-D quasigeostrophic convection model (QGCM) (e.g. Cardin & Olson 1994; Aubert *et al.* 2003; Morin & Dormy 2004, 2006; Gillet & Jones 2006; Gillet *et al.* 2007) to examine the effects of CMB topography on the convective dynamics of the core. The use of the QGCM allows us to reach lower Ekman number and higher Reynolds number flows than is possible in most 3-D models of core convection. Furthermore, recent work examining the time-varying geomagnetic field supports the idea that the large scale motions of the core are dominated by quasigeostrophic dynamics (Schaeffer & Pais 2011).

As with previous studies of topographic effects on core dynamics (Bassom & Soward 1996; Bell & Soward 1996; Herrmann & Busse 1998; Westerburg & Busse 2003), we do not consider the effects of a magnetic field in the present work. Cardin & Olson (1995) employed the QGCM without boundary topography to show that a magnetic field can significantly reduce the amplitude of the zonal flow. Their results also showed that a magnetic field of sufficient strength can cause a reversal of the zonal flow direction. Focusing on the non-magnetic case with a single topographic feature thus allows us to isolate the most basic response of the system, and will provide a useful comparison for the more complicated case of magnetoconvection with boundary topography that will be investigated in future work.

We fix the topographic width and fluid properties, although varying the rotation rate of the system, the thermal driving strength and the topographic amplitude. Our results show that the presence of the topography results in the excitation of a stationary topographic Rossby wave. The wave generates a strongly longitudinally dependent heat flux, and an increase in the strength of the zonal flow. For the first time, we show that, even in the presence of convective turbulence, topography on the CMB can create flow structures that remain fixed relative to the mantle. Section 2 presents the QGCM and the numerical methods used for solving the governing equations. In Section 3, we present our results, and in Section 4 we discuss the implications for the Earth's core.

2 METHODOLOGY

We extend the QGCM used by previous authors (Cardin & Olson 1994; Aubert *et al.* 2003; Morin & Dormy 2004, 2006; Gillet & Jones 2006; Gillet *et al.* 2007) with the inclusion of non-axisymmetric boundary topography. The QGCM is an extension of the original theory developed by Busse (1970) for convection in rapidly rotating spherical shells. The primary difference between the two models lies in the treatment of the outer bounding surfaces; the QGCM employs spherical (curved) outer boundaries, whereas Busse's original asymptotic theory requires the use of small linearly sloping outer boundaries. Detailed comparison with laboratory experiments in water and liquid gallium have shown that the QGCM captures the essential qualitative dynamics of turbulent rotating convection in a spherical shell (Aubert *et al.* 2003; Gillet *et al.* 2007), even though it is not asymptotically valid in this case. The basic premise of the QGCM is that the rapid rotation results in cylindrically radial and azimuthal velocity components that are approximately invariant in the direction of the rotation axis. This property results in 'columnar' convection (see Fig. 1a) (e.g. Sprague *et al.* 2006; Grooms *et al.* 2010) that remains accurate as long as the buoyancy forcing is not too strong (Sprague *et al.* 2006; King *et al.* 2009, 2010). Assuming such a columnar flow, a 2-D vorticity streamfunction formulation can be employed in the equatorial plane, thereby resulting in substantial computational savings when compared to 3-D models.

The flow domain that we consider is shown in Fig. 1(a) and consists of a spherical shell 'section' with inner radius r_i and outer radius r_o rotating with steady angular velocity Ω. The radius ratio is fixed to $\eta = r_i/r_o = 0.30$. The equations are solved in a cylindrical

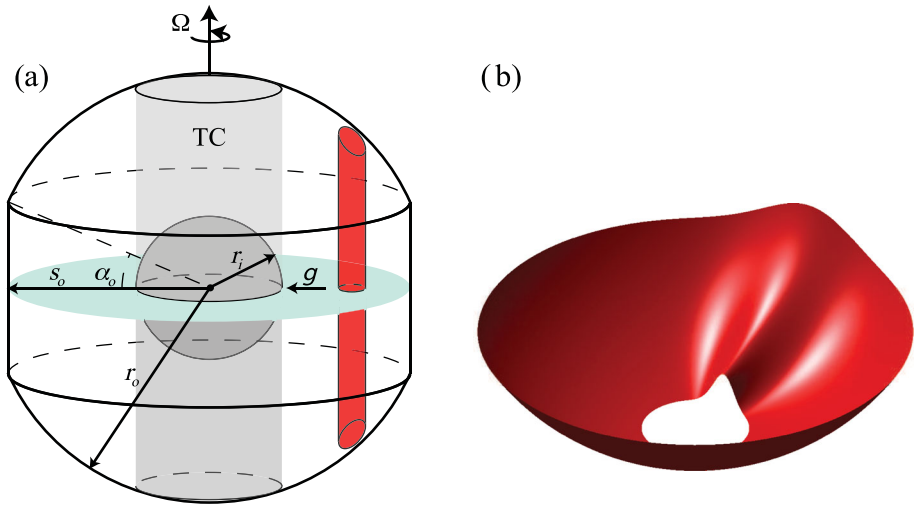

Figure 1. (a) Schematic of the flow domain used in the current study. Ω is the rotation rate of the system, g is the gravitational acceleration and r_i and r_o are the inner and outer radii, respectively. The equations are solved in the equatorial plane of outer cylindrical radius, s_o, shown in blue. The fluid motion consists of thin columnar structures, shown in red, that remain parallel to the rotation axis [adapted from Aubert *et al.* (2003)]. The tangent cylinder (TC) is shown by the shaded region tangent to the inner sphere. In this study, $\eta = r_i/r_o = 0.3$, $s_o/r_o = 0.85$. (b) Oblique view of the bottom half of the outer spherical surface with the Gaussian 'ridge' topography superposed. For clarity the amplitude of the ridge shown here is $\epsilon = -0.20$. The standard deviation of the ridge's latitudinal extent is fixed throughout this study at $\sigma = 0.3/\sqrt{2}$.

coordinate system (s, ϕ, z), where the equatorial plane is located at $z = 0$. As with previous work, flow within the tangent cylinder (TC) is not considered. (The TC is the cylindrical region tangent to the inner sphere and parallel to the rotation axis, and is shown by the shaded region in Fig. 1a.) In this study, we consider a single Gaussian 'ridge' that extends radially across the bottom boundary as shown in Fig. 1(b). The amplitude of the ridge does not depend on cylindrical radius, s. We, therefore, exclude the equatorial region of the outer spherical surface by limiting the radial solution domain to $s \in [r_i, s_o]$ to prevent the topography from intersecting the equatorial plane. Without this restriction, the equatorial plane will no longer be circular; such domains require numerical techniques that are considerably more complex than that which we employ in the current study. Similar restrictions have been used by Yano *et al.* (2005) and Takehiro (2008) for the case of axisymmetric boundaries. Throughout this study we set $s_o = 0.85\, r_o$, such that the equatorial region is removed at a latitude of $\alpha_o = \cos^{-1}(s_o/r_o) \approx 32^\circ$.

The formulation for the QGCM outlined here expands upon that of Gillet & Jones (2006) by including the effects of non-axisymmetric boundary topography. The contained fluid is characterized by a kinematic viscosity ν, thermal diffusivity κ and thermal expansion coefficient α. The basic state is cylindrical heat conduction, with the temperature on the inner and outer boundaries held constant at T_i^* and T_o^*, respectively. Gravity is taken to vary linearly with cylindrical radius, $\mathbf{g} = -g\mathbf{s}/r_o$. The equations are non-dimensionalized using $d = r_o - r_i$ for the length scale, d^2/κ as the time scale and $\Delta T^* = T_i^* - T_o^*$ for the temperature scale. We take the basic dimensionless conductive temperature profile T_c as the solution to the equation

$$\nabla^2 T_c = 0, \tag{1}$$

with boundary conditions $T_c(r_i) = 1$ and $T_c(s_o) = 0$; where we use the notation

$$\nabla^2(\cdot) = \left[\frac{1}{s}\frac{\partial}{\partial s}\left(s\frac{\partial(\cdot)}{\partial s}\right) + \frac{1}{s^2}\frac{\partial^2(\cdot)}{\partial \phi^2}\right]. \tag{2}$$

As the QGCM is not capable of modelling the axial (z) diffusion of heat, the term $\partial^2/\partial z^2$ has been omitted in eq. (2). The solution for T_c is then given by

$$T_c(s) = \frac{\ln(s/s_o)}{\ln(r_i/s_o)}. \tag{3}$$

The temperature distribution is decomposed as $T(s, \phi, t) = T_c(s) + \theta(s, \phi, t)$, where $\theta(s, \phi, t)$ is the perturbation.

With the radial (s), azimuthal (ϕ) and vertical (z) velocity components denoted by u, v and w, respectively, the axial vorticity ζ and streamfunction ψ are defined by the relations

$$\zeta = \frac{1}{s}\frac{\partial}{\partial s}(sv) - \frac{1}{s}\frac{\partial u}{\partial \phi}, \tag{4}$$

$$\nabla^2 \psi = -\zeta, \tag{5}$$

$$u = \frac{1}{s}\frac{\partial \psi}{\partial \phi}, \qquad v = -\frac{\partial \psi}{\partial s}. \tag{6}$$

Henceforth, we shall refer to the axial vorticity simply as 'the vorticity'. Employing the Boussinesq approximation (Tritton 2001), the quasigeostrophic vorticity equation and thermal energy equation become

$$\frac{1}{Pr}\left(\frac{\partial \zeta}{\partial t} + u\frac{\partial \zeta}{\partial s} + \frac{v}{s}\frac{\partial \zeta}{\partial \phi}\right) = \frac{2}{E}\frac{\partial w}{\partial z} - Ra\frac{\partial \theta}{\partial \phi} + \nabla^2 \zeta, \tag{7}$$

$$\frac{\partial \theta}{\partial t} + u\frac{\partial \theta}{\partial s} + \frac{v}{s}\frac{\partial \theta}{\partial \phi} = -v\frac{dT_c}{ds} + \nabla^2 \theta. \tag{8}$$

We refer to the references (Cardin & Olson 1994; Aubert *et al.* 2003; Gillet & Jones 2006) for detailed derivations of eqs (7) and (8). The Prandtl number, Pr, Ekman number, E and Rayleigh number, Ra, are given by

$$Pr = \frac{\text{viscous diffusion}}{\text{thermal diffusion}} = \frac{\nu}{\kappa}, \tag{9}$$

$$E = \frac{\text{viscous forces}}{\text{Coriolis force}} = \frac{\nu}{\Omega d^2}, \tag{10}$$

$$Ra = \frac{\text{buoyancy force}}{\text{diffusion}} = \frac{g\alpha \Delta T d^3}{\nu\kappa}. \tag{11}$$

The Prandtl number is fixed at $Pr = 0.025$ throughout our investigation. This Pr value is similar to that of liquid gallium and mercury commonly used in studies of Rayleigh–Bénard and planetary core-style convection (e.g. Cioni *et al.* 2000; Aubert *et al.* 2001; Aurnou & Olson 2001; Yanagisawa *et al.* 2010), thus allowing for possible comparisons with laboratory experiments (e.g. Aubert *et al.* 2003; Gillet *et al.* 2007).

The fundamental difference between purely 2-D flows and quasi-geostrophic flows is the presence of the vortex stretching term, $(2/E)\partial w/\partial z$, on the right-hand side of eq. (7). This term involves two contributions: (1) topographic (including axisymmetric and non-axisymmetric) vortex stretching because of the change in height of the bounding surfaces with horizontal position (s, ϕ) and (2) vortex stretching because of viscous damping in the Ekman boundary layers that are present on the top and bottom solid boundaries [i.e. Ekman pumping (Greenspan 1968)]. Non-axisymmetric topographic vortex stretching is because of the presence of CMB topography, and to our knowledge has not been employed previously with the QGCM.

Although all previous work with the QGCM has employed axisymmetric topographic vortex stretching, there have been various treatments of the Ekman pumping component of vortex stretching. Cardin & Olson (1994) and Morin & Dormy (2004) omitted Ekman pumping entirely. Aubert *et al.* (2003) and Morin & Dormy (2006) included Ekman pumping only on the axisymmetric or zonal flow. Gillet & Jones (2006) and Gillet *et al.* (2007) included an isotropic Ekman pumping formulation that acts on all scales of fluid motion. Similar to Gillet & Jones (2006) and Gillet *et al.* (2007), we employ Greenspan's (1968) original formulation that does not preferentially act on certain scales. This formulation has also been applied in Busse's annulus model (Brummell & Hart 1993; Jones *et al.* 2003), and in mechanically driven flows (Schaeffer & Cardin 2005, 2006).

An expression for the vortex stretching term can be found by axially averaging eq. (7). Because the vorticity is axially invariant under the QGCM, only the vortex stretching term in eq. (7) is affected by this operation. Therefore, we focus here only on the derivation of the stretching term. The top and bottom bounding surfaces are respectively defined as

$$h_T = \sqrt{r_o^2 - s^2}, \tag{12}$$

$$h_B = -\left(\sqrt{r_o^2 - s^2} + f(\phi)\right), \tag{13}$$

where the topography is given by f and is restricted to being only a function of azimuthal position ϕ for this study. Axial integration of the stretching term gives

$$\int_{h_B}^{h_T} \frac{\partial w}{\partial z}\, dz = \frac{w_T - w_B}{h}, \tag{14}$$

where $h(s, \phi) = h_T - h_B$ is the total axial height and w_T and w_B are the vertical velocities at the top and bottom surfaces, respectively. Denoting the unit vectors in the cylindrical coordinate system as $(\hat{\mathbf{s}}, \hat{\boldsymbol{\phi}}, \hat{\mathbf{z}})$, the following kinematic conditions hold on the top and bottom boundaries

$$\mathbf{u} \cdot \hat{\mathbf{n}}_\mathbf{T} = u\ (\hat{\mathbf{n}}_\mathbf{T} \cdot \hat{\mathbf{s}}) + v\ \left(\hat{\mathbf{n}}_\mathbf{T} \cdot \hat{\boldsymbol{\phi}}\right) + w_T\ (\hat{\mathbf{n}}_\mathbf{T} \cdot \hat{\mathbf{z}}), \tag{15}$$

$$\mathbf{u} \cdot \hat{\mathbf{n}}_\mathbf{B} = u\ (\hat{\mathbf{n}}_\mathbf{B} \cdot \hat{\mathbf{s}}) + v\ \left(\hat{\mathbf{n}}_\mathbf{B} \cdot \hat{\boldsymbol{\phi}}\right) + w_B\ (\hat{\mathbf{n}}_\mathbf{B} \cdot \hat{\mathbf{z}}), \tag{16}$$

where the outward pointing surface normal unit vectors are given by

$$\hat{\mathbf{n}}_\mathbf{T} = \left[\frac{s}{r_o}, 0, \frac{h_T}{r_o}\right], \tag{17}$$

$$\hat{\mathbf{n}}_\mathbf{B} = \left[\gamma \frac{s}{\sqrt{r_o^2 - s^2}}, -\frac{\gamma}{s}\frac{\partial f}{\partial \phi}, -\gamma\right], \text{ with} \tag{18}$$

$$\gamma = \left[\frac{s^2}{r_o^2 - s^2} + \left(\frac{1}{s}\frac{\partial f}{\partial \phi}\right)^2 + 1\right]^{-1/2}. \tag{19}$$

Solving for w_T and w_B in eqs (15) and (16) gives

$$w_T = -\frac{s}{h_T}u + \frac{r_o}{h_T}\mathbf{u} \cdot \hat{\mathbf{n}}_\mathbf{T}, \tag{20}$$

$$w_B = \frac{s}{h_T}u - \frac{1}{s}\frac{\partial f}{\partial \phi}v - \frac{1}{\gamma}\mathbf{u} \cdot \hat{\mathbf{n}}_\mathbf{B}, \tag{21}$$

and the vortex stretching term can then be written as

$$\frac{\partial w}{\partial z} = \frac{w_T - w_B}{h} = -\frac{2s}{h_T h}u + \frac{1}{sh}\frac{\partial f}{\partial \phi}v + \frac{r_o}{h_T h}\mathbf{u} \cdot \hat{\mathbf{n}}_\mathbf{T} + \frac{1}{\gamma h}\mathbf{u} \cdot \hat{\mathbf{n}}_\mathbf{B}. \tag{22}$$

Greenspan's (1968) generic formula for Ekman pumping then provides expressions for $\mathbf{u} \cdot \hat{\mathbf{n}}_\mathbf{T}$ and $\mathbf{u} \cdot \hat{\mathbf{n}}_\mathbf{B}$:

$$\mathbf{u} \cdot \hat{\mathbf{n}}_{\mathbf{T,B}} = -\frac{E^{1/2}}{2}\hat{\mathbf{n}}_{\mathbf{T,B}} \cdot \nabla \times \left(\frac{\hat{\mathbf{n}}_{\mathbf{T,B}} \times \mathbf{u}}{\sqrt{|\hat{\mathbf{n}}_{\mathbf{T,B}} \cdot \hat{\mathbf{z}}|}} + \frac{(\hat{\mathbf{n}}_{\mathbf{T,B}} \cdot \hat{\mathbf{z}})\ \mathbf{u}}{|\hat{\mathbf{n}}_{\mathbf{T,B}} \cdot \hat{\mathbf{z}}|\sqrt{|\hat{\mathbf{n}}_{\mathbf{T,B}} \cdot \hat{\mathbf{z}}|}}\right), \tag{23}$$

allowing us to use eqs (22) and (23) to compute the vortex stretching term throughout the domain of our model.

The topography we consider in this study consists of a single Gaussian ridge that extends radially across the bottom boundary and is given by

$$f(\phi) = \epsilon \exp\left[-\frac{(\phi - \pi)^2}{2\sigma^2}\right], \tag{24}$$

where ϵ and σ are the amplitude and standard deviation of the topography, respectively. The standard deviation of the ridge is fixed throughout our study at $\sigma = 0.3/\sqrt{2}$; this value corresponds to a 'width' of $6\sigma \approx 73^\circ$.

Because the Ekman numbers employed in the current study are typically $\sim 9 - 10$ orders of magnitude larger than values pertaining to the core, we use non-dimensional topographic amplitudes up to two orders of magnitude larger ($0.01 \leq |\epsilon| \leq 0.10$) than what is thought to represent the CMB (i.e. $\epsilon \approx 2\,\text{km}/2000\,\text{km} \sim 10^{-3}$). This is done to compensate for the significant effects of friction in our simulations. However, it should be noted that CMB topography is approximately 10^4 times larger in amplitude than the $E^{1/2}$-thick Ekman boundary layer that is present on the CMB. In comparison, we use topographic amplitudes that are $\approx 10 - 10^2$ times larger than the Ekman layer thickness in our simulations. With this metric, our amplitudes may be considered small in comparison to those that characterize the CMB.

When $\epsilon \ll 1$, we have $\gamma \approx h_T/r_o$ and the effects of the topographic ridge on Ekman pumping can be neglected. This approximation allows for significant mathematical simplification of the Ekman

pumping formulation such that $\mathbf{u}\cdot\hat{\mathbf{n}}_{\mathbf{B}} \approx \mathbf{u}\cdot\hat{\mathbf{n}}_{\mathbf{T}}$, so that eq. (22) becomes

$$\frac{\partial w}{\partial z} = -\frac{2s}{h_T h}u + \frac{1}{sh}\frac{\partial f}{\partial \phi}v + \frac{2r_o}{h_T h}\mathbf{u}\cdot\hat{\mathbf{n}}_{\mathbf{T}}, \tag{25}$$

and eq. (23) becomes

$$\mathbf{u}\cdot\hat{\mathbf{n}}_{\mathbf{T}} = -\frac{1}{2}E^{1/2}\left(\frac{h_T}{r_o}\right)^{1/2}\left[\zeta + \frac{sv}{2h_T^2} - \frac{s}{h_T^2}\frac{\partial u}{\partial \phi} + \frac{5r_o s}{2h_T^3}u\right]. \tag{26}$$

Combining eqs (25) and (26) yields a complete description of vortex stretching in the QGCM.

No-slip boundary conditions are applied at $s = r_i$ and $s = s_o$:

$$\frac{\partial \psi}{\partial s}(r_i,\phi) = \frac{\partial \psi}{\partial s}(s_o,\phi) = 0. \tag{27}$$

No-slip boundary conditions are appropriate for modelling flow in the equatorial plane of the Earth's core, and will be useful for comparison to laboratory experiments. In addition, the zonal flow structure we observe is very similar to that reported in Cardin & Olson (1995), where a stress-free boundary condition was employed at the inner boundary. This similarity suggests that the results presented in this study are not unique to our choice of boundary conditions.

Dirichlet boundary conditions for the stream function can be found by considering the volumetric flow rate per unit axial depth of the annulus

$$\psi(s_o,\phi) - \psi(r_i,\phi) = -\int_{r_i}^{s_o} v\,\mathrm{d}s. \tag{28}$$

For simplicity, we set $\psi(r_i,\phi) = \psi_i = 0$ and azimuthally average eq. (28) to get

$$\psi(s_o,\phi) = \psi_o = -\int_{r_i}^{s_o}\langle v\rangle\,\mathrm{d}s, \tag{29}$$

where the azimuthal average operator is given by $\langle\cdot\rangle = 1/(2\pi)\int_0^{2\pi}(\cdot)\,\mathrm{d}\phi$. The relationship between $\langle v\rangle$ and the zonal vorticity, $\langle\zeta\rangle$, is then given by azimuthally averaging eq. (4) to get

$$\langle\zeta\rangle = \frac{1}{s}\frac{\partial}{\partial s}\left(s\langle v\rangle\right). \tag{30}$$

An equation for $\langle v\rangle$ is found by azimuthally averaging the ϕ-component momentum equation (e.g. Peyret 2002) to get

$$\frac{1}{Pr}\left(\frac{\partial\langle v\rangle}{\partial t} + \left\langle u\frac{\partial v}{\partial s}\right\rangle + \left\langle\frac{uv}{s}\right\rangle\right) = -\frac{2}{E}\langle u\rangle + \nabla^2\langle v\rangle - \frac{1}{s^2}\langle v\rangle. \tag{31}$$

Two effects contribute to generating a non-zero azimuthally averaged radial velocity $\langle u\rangle$: (1) circulation through the Ekman boundary layers present on the top and bottom bounding surfaces and (2) the interaction of the flow with the topographic ridge. An equation for $\langle u\rangle$ that includes the contribution from the Ekman layers and topography can be found by azimuthally averaging eq. (25)

$$\frac{\partial\langle w\rangle}{\partial z} = -\frac{2s}{h_T}\left\langle\frac{u}{h}\right\rangle + \frac{1}{s}\left\langle\frac{1}{h}\frac{\partial f}{\partial\phi}v\right\rangle + \frac{2r_o}{h_T}\left\langle\frac{\mathbf{u}\cdot\hat{\mathbf{n}}_{\mathbf{T}}}{h}\right\rangle. \tag{32}$$

Conservation of mass then gives

$$\frac{1}{s}\frac{\partial(s\langle u\rangle)}{\partial s} + \frac{\partial\langle w\rangle}{\partial z} = 0. \tag{33}$$

Combining eqs (32) and (33) leads to

$$-\frac{1}{s}\frac{\partial(s\langle u\rangle)}{\partial s} = -\frac{2s}{h_T}\left\langle\frac{u}{h}\right\rangle + \frac{1}{s}\left\langle\frac{1}{h}\frac{\partial f}{\partial\phi}v\right\rangle + \frac{2r_o}{h_T}\left\langle\frac{\mathbf{u}\cdot\hat{\mathbf{n}}_{\mathbf{T}}}{h}\right\rangle. \tag{34}$$

If we assume $\epsilon \ll 1$, then $h \approx 2h_T$ and eq. (34) simplifies to

$$-\frac{1}{s}\frac{\partial(s\langle u\rangle)}{\partial s} = -\frac{s}{h_T^2}\langle u\rangle + \frac{1}{2sh_T}\left\langle\frac{\partial f}{\partial\phi}v\right\rangle + \frac{r_o}{h_T^2}\left\langle\mathbf{u}\cdot\hat{\mathbf{n}}_{\mathbf{T}}\right\rangle. \tag{35}$$

The second term on the right-hand side of eq. (35) represents the effects of the topography on the zonal velocity; this term makes it difficult to solve for $\langle u\rangle$ explicitly. To overcome this difficulty, we employ an explicit time-stepping scheme on the Ekman pumping term appearing in eq. (31) that allows for decoupling between eqs (31) and (35). For instance, if v^n is the zonal velocity at time step n, the solution of eq. (35) gives $\langle u\rangle^n$, and eq. (31) can then be solved using standard methods.

We note that in our initial investigation the topographic stress term appearing on the right-hand side of eq. (35) was omitted in the simulations; a reviewer subsequently alerted us to this oversight. It was found that when this term was absent the zonal flow strength was observed to increase as the topographic amplitude was increased from zero. As we discuss in Section 3, however, the zonal flow strength generally decreases with topographic amplitude when the topographic stress term is included. No significant change was observed in any of the other trends reported in the present work.

To summarize, the governing equations for the QGCM are given by

$$\frac{1}{Pr}\left(\frac{\partial\zeta}{\partial t} + u\frac{\partial\zeta}{\partial s} + \frac{v}{s}\frac{\partial\zeta}{\partial\phi}\right) = \frac{2}{E}\frac{\partial w}{\partial z} - Ra\frac{\partial\theta}{\partial\phi} + \nabla^2\zeta, \tag{36}$$

$$\nabla^2\psi = -\zeta, \tag{37}$$

$$u = \frac{1}{s}\frac{\partial\psi}{\partial\phi}, \qquad v = -\frac{\partial\psi}{\partial s} \tag{38}$$

$$\frac{1}{Pr}\left(\frac{\partial\langle v\rangle}{\partial t} + \left\langle u\frac{\partial v}{\partial s}\right\rangle + \left\langle\frac{uv}{s}\right\rangle\right) = -\frac{2}{E}\langle u\rangle + \nabla^2\langle v\rangle - \frac{1}{s^2}\langle v\rangle, \tag{39}$$

$$\frac{\partial\theta}{\partial t} + u\frac{\partial\theta}{\partial s} + \frac{v}{s}\frac{\partial\theta}{\partial\phi} = -u\frac{\mathrm{d}T_c}{\mathrm{d}s} + \nabla^2\theta, \tag{40}$$

with the vortex stretching term, $\partial w/\partial z$, given by eqs (25) and (26), and the azimuthally averaged radial velocity, $\langle u\rangle$, given by eq. (35). The boundary conditions for this set of equations are

$$\frac{\partial\psi}{\partial s}(r_i,\phi) = \frac{\partial\psi}{\partial s}(s_o,\phi) = 0, \tag{41}$$

$$\psi_i = 0, \qquad \psi_o = -\int_{r_i}^{s_o}\langle v\rangle\,\mathrm{d}s, \tag{42}$$

$$\langle v(r_i,\phi)\rangle = \langle v(s_o,\phi)\rangle = 0, \tag{43}$$

$$\theta(r_i,\phi) = \theta(s_o,\phi) = 0. \tag{44}$$

Eqs (36) and (37) are solved subject to boundary conditions (41) and (42), eq. (39) is solved with boundary conditions (43) and the heat eq. (40) is solved with conditions (44).

The numerical solution of the governing equations is found by employing M Fourier modes in azimuth, and solving the resulting Fourier–Galerkin equations by means of a second-order accurate finite difference scheme in radius. Gauss–Lobatto (Chebyshev) points are used to increase the radial resolution near the inner and outer solid boundaries

$$s_j = \frac{1}{2}\left[(s_o - r_i)\cos\frac{\pi j}{N} + s_o + r_i\right], \quad j = 0,\ldots,N, \tag{45}$$

where the total number of radial panels is N (i.e. the total number of radial grid points is $N+1$). A second-order Adams–Bashforth/backward differentiation scheme is used to advance the solution in time. We employ the influence matrix method

to account for the lack of boundary conditions on the vorticity (Peyret 2002); a similar methodology was recently applied in a study of mechanically driven flows in a spherical shell geometry (Calkins *et al.* 2010).

2.1 Relevant physical concepts

2.1.1 Potential vorticity and geostrophic contours

The expression for the axial stretching (25) can be rewritten as

$$\frac{\partial w}{\partial z} = \frac{1}{h}\mathbf{u_{2D}} \cdot \nabla_{\mathbf{2D}} h + \frac{2r_o}{h_T h}\mathbf{u} \cdot \hat{\mathbf{n}}_{\mathbf{T}}, \tag{46}$$

where the 2-D horizontal velocity vector is $\mathbf{u_{2D}} = (u, v)$, and

$$\nabla_{\mathbf{2D}}(\cdot) = \hat{\mathbf{s}}\,\frac{\partial}{\partial s}(\cdot) + \hat{\phi}\,\frac{1}{s}\frac{\partial}{\partial \phi}(\cdot). \tag{47}$$

Substitution of (46) into the vorticity eq. (36) yields

$$\frac{\mathrm{D}}{\mathrm{Dt}}\left(\frac{\zeta}{Pr} - \frac{2}{E}\ln h\right) = \left(\frac{4r_o}{E}\right)\frac{\mathbf{u}\cdot\hat{\mathbf{n}}_{\mathbf{T}}}{h_T h} - Ra\frac{\partial\theta}{\partial\phi} + \nabla^2\zeta, \tag{48}$$

where the material derivative D/Dt is given by

$$\frac{\mathrm{D}}{\mathrm{Dt}}(\cdot) = \frac{\partial}{\partial t}(\cdot) + \mathbf{u_{2D}} \cdot \nabla_{\mathbf{2D}}(\cdot). \tag{49}$$

The quantity $q = \zeta/Pr - (2/E)\ln h$ is referred to as the potential vorticity. The terms on the right-hand side of (49) represent Ekman pumping, thermal buoyancy and internal friction, respectively. In the absence of external and internal forces (including Ekman pumping), eq. (48) becomes

$$\frac{\mathrm{D}}{\mathrm{Dt}}\left(\frac{\zeta}{Pr} - \frac{2}{E}\ln h\right) = \frac{\mathrm{Dq}}{\mathrm{Dt}} = 0, \tag{50}$$

expressing the fact that q is a conserved quantity that is advected with the flow field. We see that the stretching term $-(2/E)\ln h$ becomes larger for smaller values of the Ekman number, showing that the shape of the boundaries becomes more important as $E \to 0$.

The tendency for quasigeostrophic flows to conserve potential vorticity results in the occurrence of a low-frequency (i.e. $\ll\Omega$) subset of inertial waves known as Rossby waves (Greenspan 1968). To illustrate the basic mechanism of Rossby wave propagation, consider an annular ring of axial fluid columns with height h_{eq} possessing zero initial vorticity and located at the 'equilibrium' radius r_{eq}, such that $q_{\mathrm{eq}} = -(2/E)\ln h_{\mathrm{eq}}$. Displacing a single fluid column radially outwards to radius r_+ results in a shortening of the column height to h_+, giving $q_+ = \zeta_+/Pr - (2/E)\ln h_+$. However, eq. (50) requires that $q_{\mathrm{eq}} = q_+$, such that $\zeta_+ = (2Pr/E)\ln(h_+/h_{\mathrm{eq}})$, implying that the fluid column acquires negative vorticity (as $h_+ < h_{\mathrm{eq}}$) as it is displaced radially outwards. Similarly, an adjacent fluid column that is displaced radially inwards will acquire positive vorticity. The velocity field associated with the positive (i.e. cyclonic) vortex is counterclockwise, resulting in a positive (i.e. prograde) azimuthal velocity field near the equilibrium position r_{eq}. Likewise, the azimuthal velocity field associated with the negative (i.e. anticyclonic) vortex near the equilibrium position is also prograde. The net effect of these disturbances around the annulus is a mean prograde drift near r_{eq}, representing a travelling Rossby wave (e.g. see fig. 5.4 of Vallis 2006).

If we now consider steady, linear motions, eq. (50) simplifies to

$$\mathbf{u_{2D}} \cdot \nabla_{\mathbf{2D}} h = 0. \tag{51}$$

This relationship states that fluid columns travel along lines of constant height when temporal variations and non-linearities are weak; such motion is referred to as geostrophic flow. Lines on which $h = constant$ are known as geostrophic contours (Greenspan 1968). For a spherical shell, the geostrophic contours are circles of constant radius centred along the rotation axis. Fig. 2 shows the contours associated with the topographic ridge considered in this study. In flows with finite inertia, Rossby waves can be excited and tend to oscillate about the geostrophic contours.

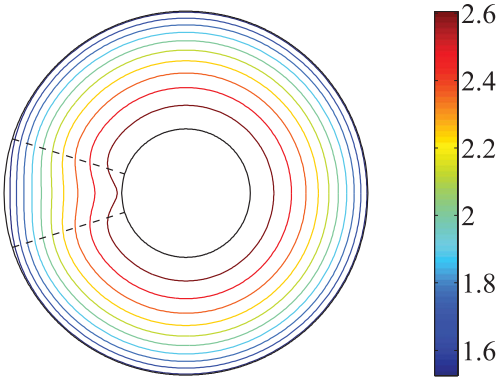

Figure 2. Geostrophic contours for the Gaussian ridge employed in the current study. The outline of the ridge is shown by the dashed black lines and the topographic amplitude is $\epsilon = -0.10$. The colour bar shows the non-dimensional axial height.

2.1.2 Rossby wave resonance

As will be discussed in Section 3, the interaction of a retrograde zonal flow with the topographic ridge results in the excitation of Rossby waves. A steady Rossby wave results when the (steady) zonal flow velocity $\overline{v}$ is equal and opposite to the phase speed of the wave. To aid in discussing some of the results of our study, we will briefly present some of the important features of linear Rossby wave resonance with the ridge. Many of the elements in the discussion that follows can be found in the text by Vallis (2006).

Neglecting temporal variations and linearizing eq. (50) about the basic state $\overline{v}$ with topography $h = \langle h\rangle + \tilde{h}$ yields

$$\frac{1}{Pr}\left(\frac{\overline{v}}{s}\frac{\partial\tilde{\zeta}}{\partial\phi}\right) - \frac{2}{E\langle h\rangle}\left(\tilde{u}\frac{\partial\langle h\rangle}{\partial s} + \frac{\overline{v}}{s}\frac{\partial\tilde{h}}{\partial\phi}\right) = 0\,, \tag{52}$$

where all non-axisymmetric components are assumed to be small (i.e. $\tilde{h} \ll \langle h\rangle$). To further simplify the analysis, let us evaluate all terms related to the column height h at mid-radius $s_{\mathrm{mid}} = (s_o + r_i)/2$, and approximate a Cartesian coordinate system as $s \to x$, $s\phi \to y$ such that

$$\frac{1}{Pr}\left(\overline{v}\frac{\partial\tilde{\zeta}}{\partial y}\right) - \frac{2}{E}\left(\beta\tilde{u} + \frac{\overline{v}}{\langle h\rangle_{\mathrm{mid}}}\frac{\partial\tilde{h}}{\partial y}\right) = 0\,, \tag{53}$$

where the slope of the outer spherical surface is denoted as $\beta = (1/\langle h\rangle_{\mathrm{mid}})\partial\langle h\rangle/\partial x$. Under this approximation, the zonal flow is now directed along the y-axis. By assuming solutions of the form $\tilde{\psi} = \hat{\psi}\exp[i(kx + ly)]$ and $\tilde{h} = \hat{h}\exp[i(kx + ly)]$, and using the relations $\nabla^2\tilde{\psi} = -\tilde{\zeta}$ and $\tilde{u} = \partial\tilde{\psi}/\partial y$, eq. (53) gives the following relationship

$$\hat{\psi} = \frac{\left(\frac{2\overline{v}}{E\langle h\rangle_{\mathrm{mid}}}\right)}{\left(\frac{\overline{v}}{Pr}L^2 - \frac{2\beta}{E}\right)}\hat{h}, \tag{54}$$

where $L^2 = k^2 + l^2$. This relationship gives us the Fourier components of the linear flow response, $\hat{\psi}$, to the presence of non-axisymmetric boundary topography with Fourier components $\hat{h}$.

Examination of the denominator in eq. (54) shows that an infinite response (i.e. resonance) occurs when

$$L = \pm\sqrt{\frac{2\beta}{E}\frac{Pr}{\overline{v}}}, \tag{55}$$

which we denote as the resonant wavenumber, L_R. Defining the zonal Reynolds number as $Re_z = \overline{v}/Pr$, and noting that the zonal Rossby number is given by $Ro = Re_z E$, the resonant wavenumber is then given by

$$L_R = \pm\sqrt{\frac{2\beta}{Ro}}. \tag{56}$$

Eq. (56) can also be written in terms of wavelength as

$$\lambda_R = 2\pi\sqrt{\frac{Ro}{2\beta}}\,. \tag{57}$$

Note that for the spherical geometry considered in this study, $\beta < 0$, which corresponds to Rossby waves that propagate in the prograde direction. The Rossby number can take both signs, where a positive value corresponds to a prograde zonal flow and a negative value corresponds to a retrograde zonal flow. For $Ro < 0$, we have a purely real-valued resonant wavenumber which corresponds to a stationary Rossby wave. In contrast, for a prograde zonal flow with $Ro > 0$ we have

$$L_{R,Ro>0} = \pm\sqrt{\frac{2|\beta|}{|Ro|}}\,i, \tag{58}$$

which corresponds to exponentially decaying and growing solutions in space, for which no stationary wave is possible (Pedlosky 1987). Thus, resonant, stationary Rossby waves can only exist when the zonal flow is retrograde in our geometry.

Although, many simplifications have been employed to develop eqs (56) and (57), the correct physical response is retained: larger Rossby number flows resonate with larger wavelength topography; smaller Rossby number flows resonate with smaller wavelength topography. This behaviour is essentially a Doppler shift, and occurs because the zonal flow stretches the wave motion over a larger distance. The streamfunction topography relationship given by eq. (54) shows that resonance between the zonal flow and topography will always occur provided h is composed of a range of topographic wavelengths. The Gaussian ridge employed in the current study has this advantage over single-wavelength sinusoidal topography (e.g. Bell & Soward 1996; Herrmann & Busse 1998). The boundary topography excites the Rossby wave, but it does not provide the restoring force. Instead, this is accomplished primarily by the stretching because of the spherical boundary shape, expressed in the term β. Because of this, the resonant mode does not depend upon the width, or standard deviation, σ, of the ridge in (56). In addition, eq. (56) demonstrates that the resonant wavenumber does not depend upon the topographic amplitude ϵ.

2.2 Relevant physical quantities

We will refer to several quantities that are useful in characterizing the properties of the flow field and heat transfer. All time-averaged quantities are denoted by an overline, $\overline{(\cdot)}$, and fluctuations are denoted by $(\cdot)'$. The temperature perturbation can, for example, be decomposed as $\theta = \overline{\theta} + \theta'$. The zonal (i.e. axisymmetric) and non-zonal kinetic energy densities are given, respectively, by

$$KE_z = \frac{1}{2A}\int_A \langle v\rangle^2 \,\mathrm{dA}, \tag{59}$$

$$KE_{nz} = \frac{1}{2A}\int_A (\tilde{u}^2 + \tilde{v}^2)\,\mathrm{dA}, \tag{60}$$

where the area of the domain is simply $A = \pi(s_o^2 - r_i^2)$, and $\tilde{u}$ and $\tilde{v} = v - \langle v\rangle$ are the non-zonal velocity components. The total kinetic energy, KE, is then defined as $KE = KE_z + KE_{nz}$. Zonal and convective Reynolds numbers are evaluated using the rms velocites:

$$Re_z = \frac{\sqrt{2\overline{KE}_z}}{Pr}, \tag{61}$$

$$Re_c = \frac{\sqrt{2\overline{KE}_{nz}}}{Pr}. \tag{62}$$

To quantify the level of thermal forcing, we will refer to the supercritical Rayleigh number

$$\widehat{Ra} = \frac{Ra}{Ra_{\mathrm{cr}}}, \tag{63}$$

where the Ra_{cr} is the critical Rayleigh number at which convective motions begin.

The heat transferred across the flow domain is measured by the Nusselt number evaluated at the inner boundary

$$Nu_i = 1 + r_i \log\left(\frac{r_i}{s_o}\right)\frac{\partial\theta}{\partial s}\Big|_{r_i}, \tag{64}$$

or at the outer boundary

$$Nu_o = 1 + s_o \log\left(\frac{r_i}{s_o}\right)\frac{\partial\theta}{\partial s}\Big|_{s_o}. \tag{65}$$

In the absence of internal sources or sinks of energy, we have $\langle\overline{Nu}_i\rangle = \langle\overline{Nu}_o\rangle = \langle\overline{Nu}\rangle$. The longitudinal variation in heat transfer along the inner and outer boundary will be measured by the fractional Nusselt numbers

$$\delta Nu_i = \frac{\overline{Nu}_i - \langle\overline{Nu}\rangle}{\langle\overline{Nu}\rangle}, \text{ and} \tag{66}$$

$$\delta Nu_o = \frac{\overline{Nu}_o - \langle\overline{Nu}\rangle}{\langle\overline{Nu}\rangle}. \tag{67}$$

The maximum values are then given by

$$\delta Nu_{i,\max} = \frac{|\overline{Nu}_i - \langle\overline{Nu}\rangle|}{\langle\overline{Nu}\rangle}, \text{ and} \tag{68}$$

$$\delta Nu_{o,\max} = \frac{|\overline{Nu}_o - \langle\overline{Nu}\rangle|}{\langle\overline{Nu}\rangle}. \tag{69}$$

The numerical resolution and various physical quantities for each of the simulations reported in the current study are given in Table 1.

3 RESULTS

3.1 Flow characteristics

The critical azimuthal wavenumber, m_{cr}, and critical Rayleigh number, Ra_{cr}, that characterize the onset of convective motion are determined by solving the linear governing equations for the two Ekman numbers employed in this study. We consider the fluid to be convectively unstable when the kinetic energy grows with time. When no topography is present (i.e. $\epsilon = 0$), we have $m_{\mathrm{cr}} = 7$ and $Ra_{\mathrm{cr}} = 5.58 \times 10^5$ for $E = 10^{-5}$, and $m_{\mathrm{cr}} = 12$ and $Ra_{\mathrm{cr}} = 7.94 \times 10^6$ for $E = 10^{-6}$. In agreement with previous work (Bell & Soward 1996), we find a finite mean flow at onset

Table 1. Summary of the numerical simulations used in this study. The number of radial panels and Fourier modes are denoted by N and M, respectively. The supercritical Rayleigh number is given by $\widehat{Ra} = Ra/Ra_{\rm cr}$. The time-averaged convective Reynolds number and zonal Reynolds number are denoted as $\overline{Re}_c$ and $\overline{Re}_z$, respectively. The time and azimuthally averaged Nusselt number is $\langle\overline{Nu}\rangle$. The maximum percentage relative variation in Nusselt number along the inner and outer boundaries are denoted by $\delta Nu_{i,\max}$ and $\delta Nu_{o,\max}$, respectively. The radius ratio, outer cylindrical radius and Prandtl number are fixed at $\eta = 0.3$, $s_o = 0.3r_o$ and $Pr = 0.025$, respectively.

E	$\widehat{Ra}$	ϵ	N	M	$\overline{Re}_c$	$\overline{Re}_z$	$\langle\overline{Nu}\rangle$	$\delta Nu_{i,\max}$ (per cent)	$\delta Nu_{o,\max}$ (per cent)
10^{-5}	2	0	160	512	252	187	1.04	–	–
10^{-5}	8	0	320	848	2.22×10^3	2.90×10^3	1.96	–	–
10^{-5}	2	−0.1	160	512	544	297	1.16	53	26
10^{-5}	4	−0.1	288	672	978	1.15×10^3	1.44	43	21
10^{-5}	8	−0.1	320	848	2.71×10^3	2.70×10^3	2.20	30	21
10^{-6}	2	0	320	700	722	635	1.09	–	–
10^{-6}	2	−0.1	384	880	1.29×10^3	769	1.24	101	17
10^{-6}	4	−0.1	480	1280	3.60×10^3	2.25×10^3	1.81	79	19
10^{-6}	8	0	400	1800	4.51×10^3	7.0×10^3	2.09	–	–
10^{-6}	8	−0.01	512	2240	4.56×10^3	6.86×10^3	2.04	9.3	11
10^{-6}	8	−0.025	512	2240	4.93×10^3	6.92×10^3	2.19	22	11
10^{-6}	8	−0.05	512	2240	5.83×10^3	6.82×10^3	2.44	38	14
10^{-6}	8	−0.075	512	2240	7.09×10^3	6.25×10^3	2.76	47	19
10^{-6}	8	−0.1	512	2240	8.06×10^3	5.71×10^3	3.08	55	28
10^{-6}	8	0.1	640	2240	7.29×10^3	6.10×10^3	2.83	48	29

and observe a change in $Ra_{\rm cr}$ with the presence of the ridge. With a topographic amplitude of $\epsilon = -0.10$, we obtain $Ra_{\rm cr} = 5.78 \times 10^5$ for $E = 10^{-5}$ and $Ra_{\rm cr} = 8.17 \times 10^6$ for $E = 10^{-6}$. For simplicity, however, the supercritical Rayleigh number $\widehat{Ra} = Ra/Ra_{\rm cr}$ will be based upon the critical Rayleigh number when no topography is present.

Fig. 3 presents snapshots in time of vorticity in the equatorial plane at $E = 10^{-5}$ for two different Rayleigh numbers and for cases without and with topography. The azimuthally averaged zonal flow profiles are superimposed on each figure; the flow is predominantly retrograde, with a weaker prograde jet near the outer boundary. This zonal flow behaviour is consistent with all previous work at low Prandtl number (Aubert *et al.* 2001, 2003; Gillet & Jones 2006; Gillet *et al.* 2007). For $\widehat{Ra} = 2$, vortical flow is most pronounced in the vicinity of the topographic ridge and the downstream region where the retrograde flow travels past the ridge. The topography acts to increase the azimuthal heterogeneity in the flow field by creating a localized region of intense convection. At $\widehat{Ra} = 2$, we see a 116 per cent increase in $\overline{Re}_c$ and a 59 per cent increase in $\overline{Re}_z$. As shown in Figs 3(c) and (d), when the supercriticality is increased to $\widehat{Ra} = 8$, the effects of the topography become less pronounced at this Ekman number. At $\widehat{Ra} = 8$, inertial effects become more apparent, with the flow field characterized by 4–6 large cyclonic (positive) vortices near the outer boundary and the same number of smaller anticyclonic vortices attached to the hot inner boundary (cyclonic vortices are shown in red; anticyclonic vortices are shown in blue). (Movies for the cases shown in Figs 3(c) and (d) are available online in the Supporting Information.) The presence of the ridge at $E = 10^{-5}$ and $\widehat{Ra} = 8$ results in a slight increase in the convective Reynolds numbers from $\overline{Re}_c = 2220$ at $\epsilon = 0$ to $\overline{Re}_c = 2710$ at $\epsilon = -0.10$. These values correspond to a percentage increase in the non-zonal Reynolds number of 22 per cent when topography is present. Conversely, we observe an 8 per cent decrease in the zonal Reynolds number for the topographic case at $\widehat{Ra} = 8$.

Fig. 4 shows cases equivalent to those in Fig. 3 for $E = 10^{-6}$. The observed percentage changes in the convective and zonal Reynolds numbers are 79 per cent and 21 per cent at $\widehat{Ra} = 2$ and 79 per cent and −18 per cent at $\widehat{Ra} = 8$ for the topographic cases. These values suggest that for lower Ekman numbers the topography can influence the flow field for a broader range of Rayleigh numbers. Comparison of Figs 4(c) and (d) shows that the topographic case is characterized by more localized peaks in vorticity with the appearance of small scale cyclonic vortices. (Movies for the cases shown in Figs 4(c) and (d) are available online in the Supporting Information.) The movie for the topographic case shows that many of the small scale cyclonic vortices are generated along the inner boundary in the lee region of the topography, where the retrograde jet detaches from the inner boundary. The cyclonic vortices often become encapsulated by a region of anticyclonic vorticity as they travel radially outwards. 'Shielded' vortices of this type have also been observed in numerical simulations of rapidly rotating convection in a plane fluid layer (Sprague *et al.* 2006). The presence of a shield greatly reduces interactions between small scale cyclonic vortices and surrounding vortical structures. This results in an increased lifespan when compared to unshielded structures.

Time-averaged stream function contours are shown in Fig. 5 for selected cases presented in Figs 3 and 4. When no topography is present, the time-averaged flow is purely azimuthal and results in the circular streamlines shown in Figs 5(a) and (d) for $E = 10^{-5}$ and $E = 10^{-6}$, respectively. The topographic cases (Figs 5b, c, e and f) show that the presence of the ridge results in the excitation of a standing Rossby wave. Similar waves have also been observed in the study of Herrmann & Busse (1998). At $\widehat{Ra} = 2$, Figs 5(b) and (e) clearly show the stationary wave. Associated with the stationary Rossby wave are local regions characterized by circular streamlines, which we refer to as eddies. The eddies near the inner boundary rotate anticyclonically and the outer eddies rotate in a cyclonic sense. Although both topographic cases at $\widehat{Ra} = 8$ exhibit eddies in the vicinity of the topography, the $E = 10^{-6}$ (Fig. 5f) case shows a larger number of stronger eddies in comparison to the $E = 10^{-5}$ (Fig. 5c) case. These standing eddies are the result of the Rossby wave whose amplitude is observed to increase with decreasing E (i.e. lower viscous damping) for a given supercriticality.

Table 2 and Fig. 6 give the average Rossby number for the retrograde jet near the inner boundary, Ro, and the 'observed' azimuthal resonant wavenumber, $L_{\rm obs}$, determined from the topographic

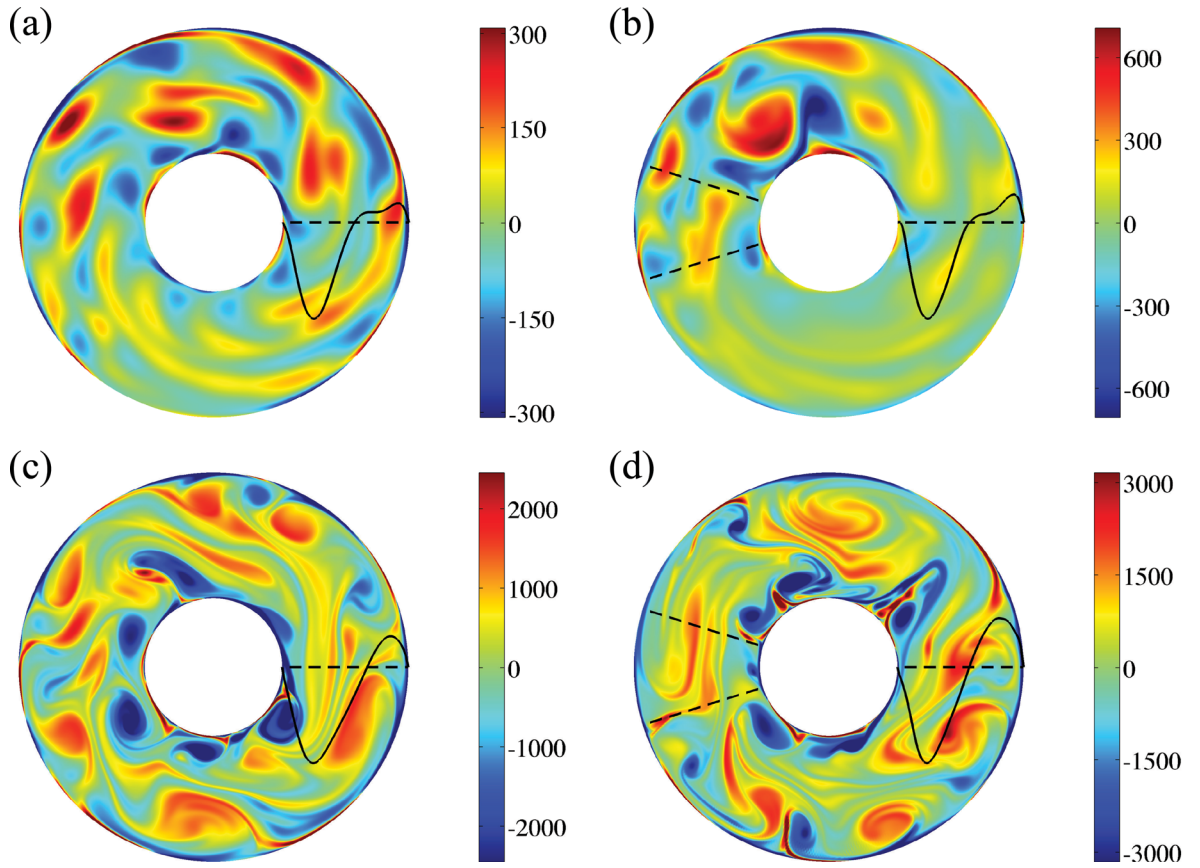

Figure 3. Instantaneous vorticity in the equatorial plane for $E = 10^{-5}$ and (a) $\widehat{Ra} = 2$, $\epsilon = 0$; (b) $\widehat{Ra} = 2$, $\epsilon = -0.10$; (c) $\widehat{Ra} = 8$, $\epsilon = 0$ and (d) $\widehat{Ra} = 8$, $\epsilon = -0.10$. The outline of the topographic ridge is shown in by the angled, dashed black lines in the 9 o'clock region and the azimuthally averaged zonal velocity profile is shown by the solid black curve. Cyclonic vortices are shown in red; anticyclonic vortices are shown in blue. Movies for cases (c) and (d) are available online.

simulations, along with the predicted value, L_R, from eq. (56) based on Ro. $L_{\rm obs}$ was determined by finding the dominant wavenumber (excluding the axisymmetric mode $m = 0$) in the time-averaged retrograde flow field. The absolute value of the predicted resonant wavenumber, $|L_R|$, was found by evaluating the slope parameter $\beta = (1/h)\partial h/\partial s$ (with $\epsilon = 0$) at r_i and rounding $|L_R|$ to the nearest integer value. In agreement with eq. (56), the values of $L_{\rm obs}$, denoted by circles in Fig. 6, do not depend strongly on the Ekman number. The effect of friction is to reduce the amplitude of the resonant mode rather than alter the wavenumber. We can see evidence of this effect by comparison of the two cases shown in Figs 5(b) and (f) that are characterized by comparable Rossby numbers, where the resonant mode is characterized by a slightly larger amplitude in the $E = 10^{-6}$ case (Fig. 5d). Table 2 shows, however, that these two cases are characterized by $L_{\rm obs} \approx 6$ because of their similar Rossby numbers.

Comparison of the last two columns in Table 2 shows that eq. (56) systematically overpredicts the resonant wavenumber. The largest difference between the observed and predicted values occurs at $E = 10^{-6}$ for $\widehat{Ra} = 2$, where $|L_R|/L_{\rm obs} \approx 2.3$. In Fig. 6, we plot the observed resonant wavenumber $L_{\rm obs}$ and the predicted resonant wavenumber $|L_R|$ for the data given in Table 2. Although, we have only three different simulations for each Ekman number, we see that $L_{\rm obs}$ does follow the predicted trend of decreasing wavenumber with increasing Rossby number. We also note that the agreement between observed and predicted resonant wavenumber becomes better as the Rossby number increases (i.e. for larger $\widehat{Ra}$); this observation is likely because of the concomitant increase in Reynolds number. Because viscous effects were neglected in the derivation of eq. (56), we expect L_R to provide a better estimate as the Reynolds number increases. Nevertheless, an investigation that considers a broader range of Rayleigh numbers is necessary to effectively test the $L_R \sim Ro^{-1/2}$ scaling. Lower Ekman number simulations are thus required to reach higher Reynolds numbers whereas maintaining relatively low Rossby numbers.

A magnified view of the region 'downstream' of the ridge is shown in Fig. 7 for the case $E = 10^{-6}$, $\widehat{Ra} = 8$ and $\epsilon = -0.10$. (A movie of the dynamics in this region is included online in the Supporting Information.) As fluid parcels in the retrograde jet encounter the topography, conservation of potential vorticity requires them to approximately follow the geostrophic contours of the ridge towards the inner boundary (see Fig. 2). The geostrophic contours on the ridge near r_i are cut-off by the inner boundary. As a result, the retrograde jet impinges on the boundary, causing the cross-section of the jet to narrow and the jet's magnitude to increase (*cf.* Fig. 5f). After travelling over the topography, the fluid travels radially outwards along the geostrophic contours. Inertia causes the fluid parcels to overshoot their equilibrium position, resulting in the excitation of the topographic Rossby wave. The wavy, thick dashed line shown in Fig. 7 approximates the pattern of this Rossby wave. The outward radial motion of the jet in the lee region of the topography results in an anticyclonic (shown in blue) recirculating eddy, or 'separation bubble', where the jet detaches from the inner boundary. The strong shear present within this eddy results in the 'roll-up' of cyclonic vortices along the inner core boundary (ICB), which are pulled

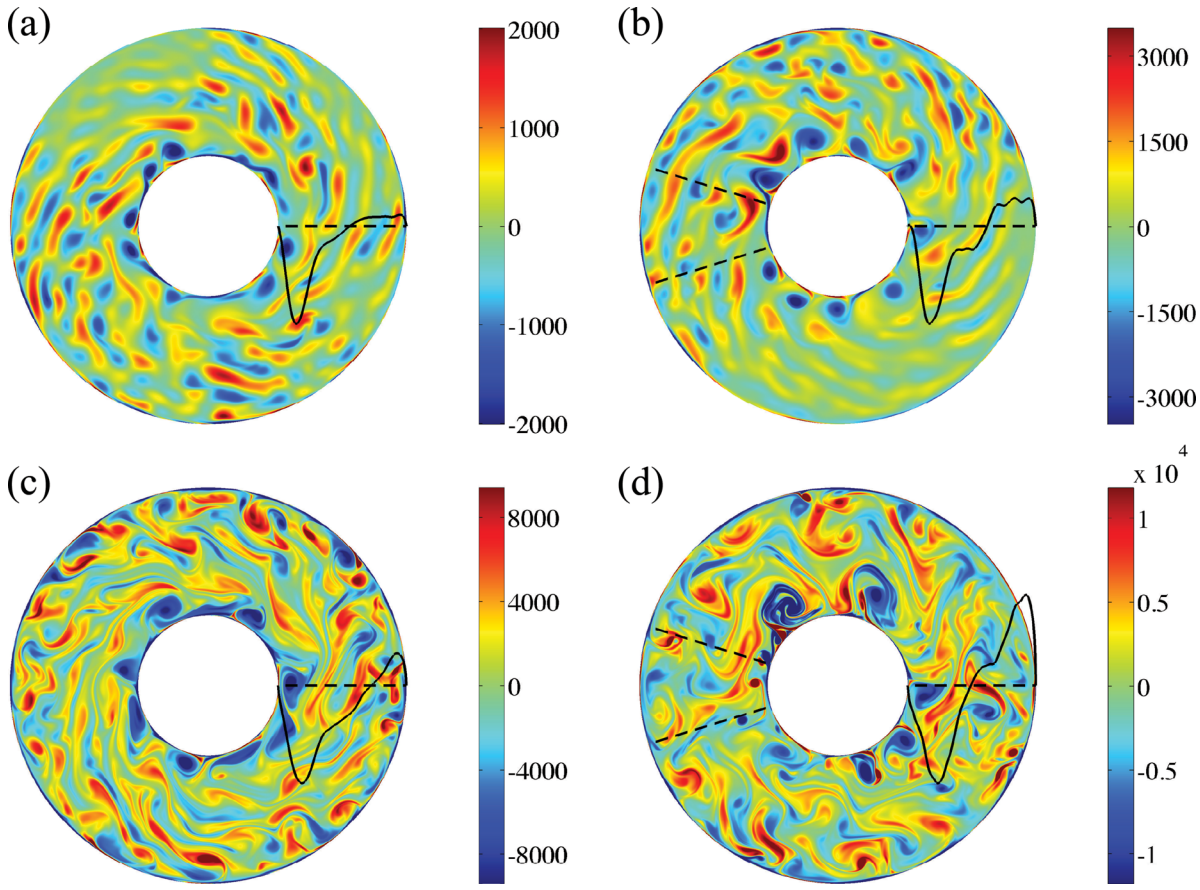

Figure 4. Instantaneous vorticity in the equatorial plane for $E = 10^{-6}$ and (a) $\widehat{Ra} = 2$, $\epsilon = 0$; (b) $\widehat{Ra} = 2$, $\epsilon = -0.10$; (c) $\widehat{Ra} = 8$, $\epsilon = 0$ and (d) $\widehat{Ra} = 8$, $\epsilon = -0.10$. The outline of the topographic ridge is shown in by the angled, dashed black lines in the 9 o'clock region and the azimuthally averaged zonal velocity profile is shown by the solid black curve. Cyclonic vortices are shown in red; anticyclonic vortices are shown in blue. Movies for cases (c) and (d) are available online.

outwards and eventually advected away by the mean flow. Strong shear is also present along the boundary of the Rossby wave, where the azimuthal velocity approaches zero. This results in elongated vortical regions that persist over time. It is common for vortices encountering these regions to be sheared out into long tendrils, thus producing the characteristic shape seen in Fig. 7 (denoted by 'strongly sheared region').

To illustrate the effects of the ridge on the strength and structure of the zonal flow, the topographic amplitude was varied systematically over the range $-0.01 \geq \epsilon \geq -0.10$ for $E = 10^{-6}$ and $\widehat{Ra} = 8$. Fig. 8(a) shows a comparison of the zonal flow profiles for five different topographic amplitudes; the control case with no topography (i.e. $\epsilon = 0$) is also shown by the dashed black line. Each of the profiles has been averaged in time and azimuth, and is given in units of the Reynolds number, $\langle \overline{v} \rangle / Pr$. The presence of the topographic ridge is observed to cause a decrease in the magnitude of the retrograde jet near the inner boundary and an increase in the magnitude of the outer prograde jet. We also see that there is an inward radial shift at the boundary between the retrograde and prograde jets (i.e. the radius at which $\langle \overline{v} \rangle = 0$). These effects increase with topographic amplitude and do not appear to saturate for the largest amplitude investigated ($\epsilon = -0.10$). Comparison of the control case and the $\epsilon = -0.10$ case shows that the peak zonal velocity in the retrograde jet decreases by approximately 33 per cent, whereas the peak velocity in the prograde jet increases by about 60 per cent. Fig. 8(b) illustrates the change in the time-averaged convective and zonal Reynolds numbers with topographic amplitude.

To determine if the sign of the topography is important in controlling the dynamics, a simulation has been carried out with a topographic ridge of positive amplitude ($\epsilon = 0.10$) at $E = 10^{-6}$ and $\widehat{Ra} = 8$. Topography with a positive amplitude represents a 'valley' on the CMB that protrudes outward into the mantle. Fig. 9(a) shows a snapshot of the vorticity with the azimuthally averaged zonal velocity. We see that the gross characteristics are similar to the equivalent case with negative topographic amplitude shown in Fig. 4(d). There is an anticyclonic eddy adjacent to the inner boundary in the lee of the topography where many of the small scale anticyclonic vortices are produced; strongly sheared vortical regions exist that trace the outline of the topographic Rossby wave (similar to the structures in Fig. 7). The primary difference for positive topographic amplitudes is that the flow in the retrograde jet initially travels radially outwards because of the reversed direction of the geostrophic contours. As illustrated in Fig. 9(b), this results in a stationary Rossby wave that is shifted towards larger radius. However, the general features of the time-averaged flow remain similar to the case with $\epsilon = -0.10$.

3.2 Heat transfer

Fig. 10 gives the time and azimuthally averaged Nusselt number for $E = 10^{-6}$ and $\widehat{Ra} = 8$ over a range of topographic amplitudes. In general, we observe an increase in the heat transfer as the topographic amplitude is increased. The increase in Nusselt number

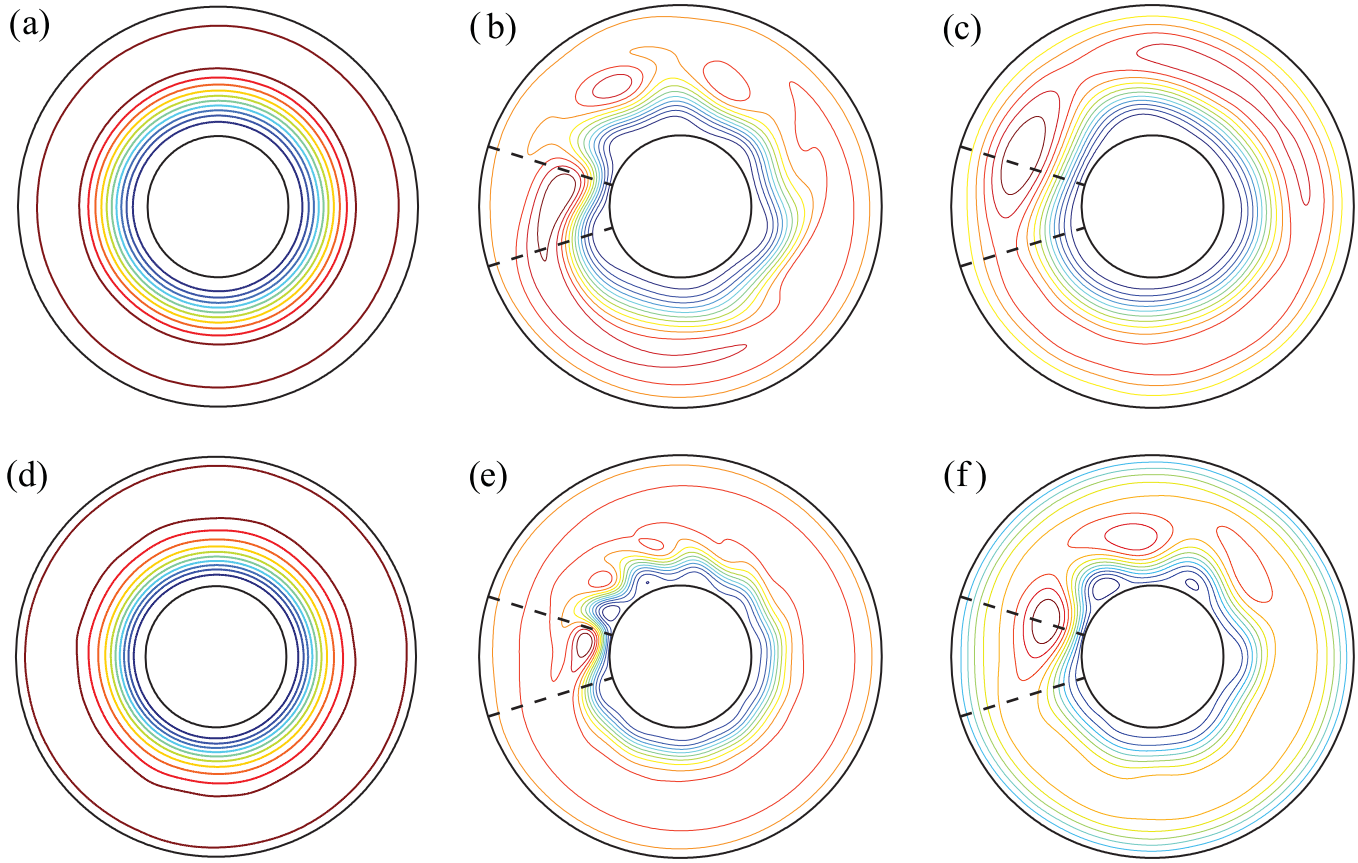

Figure 5. Time-averaged stream function contours for (a) $E = 10^{-5}$, $\widehat{Ra} = 8$, $\epsilon = 0$; (b) $E = 10^{-5}$, $\widehat{Ra} = 2$, $\epsilon = -0.10$; (c) $E = 10^{-5}$, $\widehat{Ra} = 8$, $\epsilon = -0.10$; (d) $E = 10^{-6}$, $\widehat{Ra} = 8$, $\epsilon = 0$, (e) $E = 10^{-6}$, $\widehat{Ra} = 2$ $\epsilon = -0.10$ and (f) $E = 10^{-6}$, $\widehat{Ra} = 8$, $\epsilon = -0.10$. The outline of the topographic ridge is shown by the dashed black lines. The contour line intervals vary for each plot, and were chosen to increase the visibility of the flow structures.

Table 2. Azimuthal resonant wavenumber, $L_{\rm obs}$, and Rossby number, Ro, for the topographic cases with $\epsilon = -0.10$. For comparison, the absolute value of the predicted resonant wavenumber, $|L_R|$, is also given. $|L_R|$ was rounded to the nearest integer value.

E	$\widehat{Ra}$	$-Ro$	$L_{\rm obs}$	$\lvert L_R\rvert$
10^{-5}	2	3.56×10^{-3}	6	11
10^{-5}	4	1.22×10^{-2}	4	6
10^{-5}	8	3.02×10^{-2}	3	4
10^{-6}	2	8.43×10^{-4}	10	23
10^{-6}	4	2.06×10^{-3}	7	15
10^{-6}	8	5.73×10^{-3}	6	9

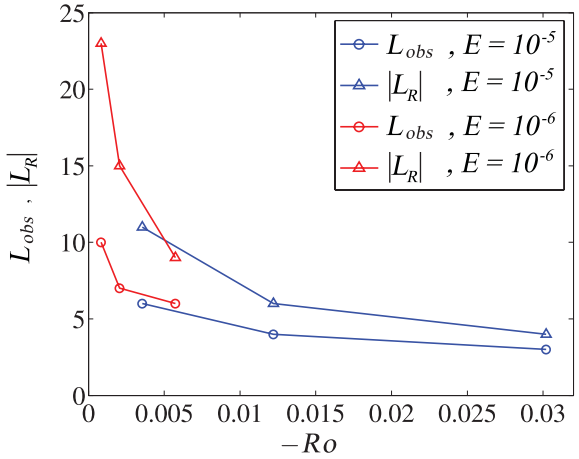

Figure 6. (a) The observed resonant wavenumber, $L_{\rm obs}$, and the predicted resonant wavenumber, L_R, as a function of the Rossby number, $-Ro$. (b) The normalized observed resonant wavenumber $L^*_{\rm obs} = L_{\rm obs}/Ro^{-1/2}$ (circles) and the normalized predicted resonant wavenumber $|L_R|^* = |L_R|/Ro^{-1/2}$ (triangles) for $E = 10^{-5}$ (blue) and $E = 10^{-6}$ (red) with $\epsilon = -0.10$.

is associated with the presence of the recirculating regions shown in Fig. 5(f), which transport heat radially outwards. The Nusselt number for the maximum topographic amplitude employed in this study, $\epsilon = -0.10$, is observed to be more than 47 per cent larger than the equivalent case without topography. In comparison, there is only a 12 per cent increase in the Nusselt number between $\epsilon = 0$ and $\epsilon = -0.10$ at $E = 10^{-5}$. This again demonstrates that the effect of friction is to reduce the effect of the topography.

To illustrate the topographically induced changes in the heat transfer, the time-averaged temperature perturbation, $\overline{\theta}$, and convective heat flux, $\overline{u'\theta'}$, are shown in Figs 11(a) and (b) for $E = 10^{-6}$, $\widehat{Ra} = 8$ and $\epsilon = -0.10$.Fig. 11(a) shows that the temperature distribution is strongly azimuthally and radially dependent, with strong perturbations present near the ridge. The wave-like nature of the disturbance excited by the topography is evident in Fig. 11(b), with strong oscillations in $\overline{u'\theta'}$ in the vicinity of the ridge.

The longitudinal dependence of the fractional relative change in the Nusselt number at the inner boundary, δNu_i, is shown in Fig. 12 for $E = 10^{-6}$ and $\epsilon = -0.10$ over the investigated range of Rayleigh

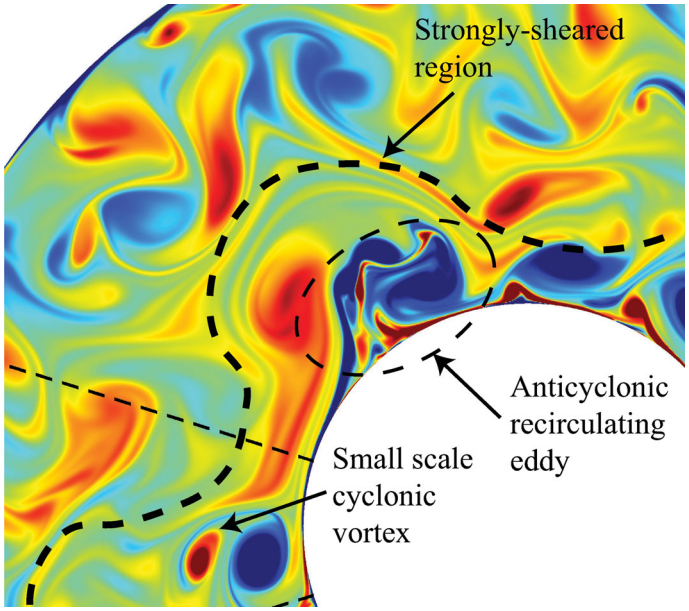

Figure 7. Close-up view of the case presented in Fig. 4(d), showing the 'downstream' region of the topography and many of the dynamical features discussed in the text. The wavy, thick dashed line traces the topographic Rossby wave pattern. Strong shear near the edge of the Rossby wave shear out many of the vortical structures into long filaments. Many of the small scale cyclonic vortices (shown in red) are shed from the region denoted by the dashed ellipse along the inner boundary. A movie is available online.

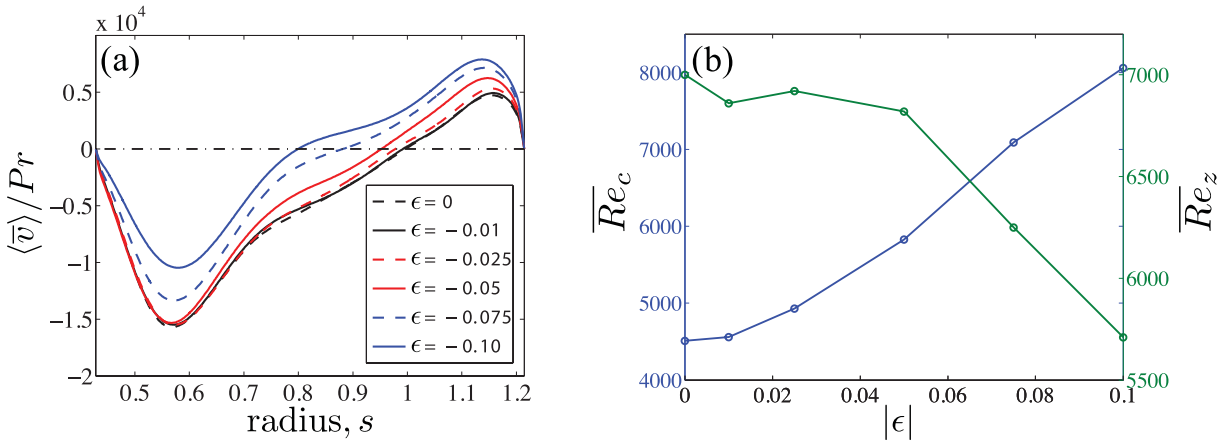

Figure 8. (a) Time and azimuthally averaged zonal velocity profiles for various topographic amplitudes. The ordinate is given in units of the local zonal Reynolds number, $\langle \overline{v} \rangle / Pr$. (b) Time-averaged convective and zonal Reynolds numbers versus topographic amplitudes. All cases are for $\widehat{Ra} = 8$ and $E = 10^{-6}$.

numbers ($\widehat{Ra} = 2, 4, 8$). For reference, the longitudinal origin of $\phi = 0^\circ$ is located at 3 o'clock with respect to equatorial plane plots such as Fig. 11. Using this reference value, longitude increases in a counterclockwise fashion around the annulus. We plot $-\phi$ along the abscissa such that the zonal flow near the inner boundary travels from left to right with respect to the figure. The centre of the topographic ridge is located at $-\phi = 180^\circ$. In terms of the interaction between the retrograde zonal flow and the topographic ridge, the 'upstream' region is from $0^\circ \leq -\phi \leq 180^\circ$, whereas the 'downstream' region is from $180^\circ \leq -\phi \leq 360^\circ$. At $\widehat{Ra} = 2$, there is a peak in heat transfer centred almost directly over the ridge, a minimum above the downstream edge of the ridge, oscillations downstream and a large region upstream of the ridge characterized by reduced heat flux relative to the azimuthally averaged value. The peak in heat transfer over the ridge at $\phi = 180^\circ$ is observed to decrease and move slightly downstream for larger values of $\widehat{Ra}$. For $\widehat{Ra} > 2$, the peak in heat transfer occurs downstream of the ridge at $\approx 240^\circ$, and is observed to occur further downstream for larger $\widehat{Ra}$. In addition, the minimum in heat transfer at the downstream edge of the ridge ($-\phi \approx 217^\circ$) appears to grow in strength and move downstream as $\widehat{Ra}$. The maximum per cent azimuthal difference in the radial heat transfer for $\widehat{Ra} = 2$, 4 and 8 is $\delta Nu_{i,\max} = 101$ per cent, 79 per cent and 55 per cent, respectively.

The maximum variation in heat transfer along the inner and outer boundary, $\delta Nu_{i,\max}$ and $\delta Nu_{o,\max}$, respectively, are given for all the topographic simulations in Table 1. In all but one of the simulations, we find the variation in heat transfer to be largest along the inner boundary (i.e. $\delta Nu_{i,\max} > \delta Nu_{o,\max}$). A steady increase in $\delta Nu_{i,\max}$ and $\delta Nu_{o,\max}$ with topographic amplitude is observed for the cases shown in Fig. 10.

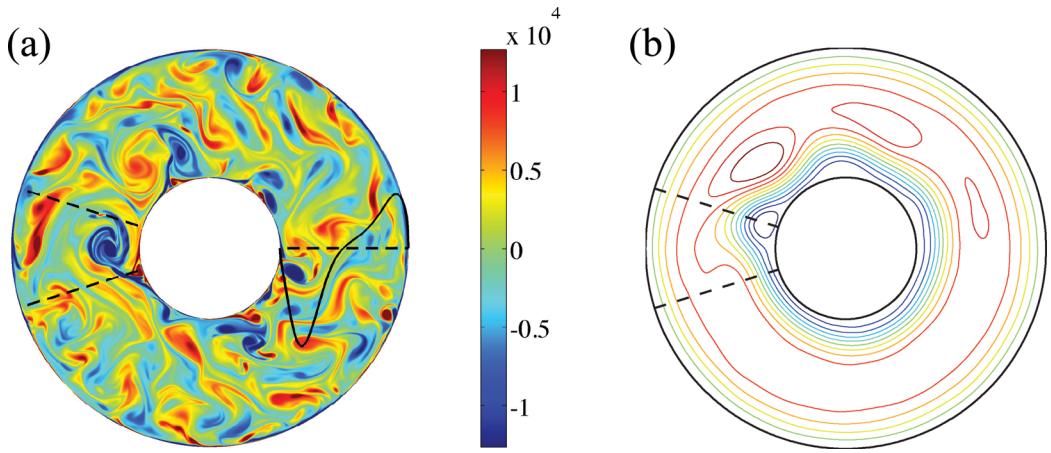

Figure 9. Case with positive topographic amplitude $\epsilon = 0.10$ at $E = 10^{-6}$ and $\widehat{Ra} = 8$. (a) Instantaneous vorticity in the equatorial plane with azimuthally averaged zonal velocity profile shown by the solid black curve and (b) time-averaged stream function contours. The outline of the topographic ridge is shown in by the angled dashed black lines in the 9 o'clock region of each figure.

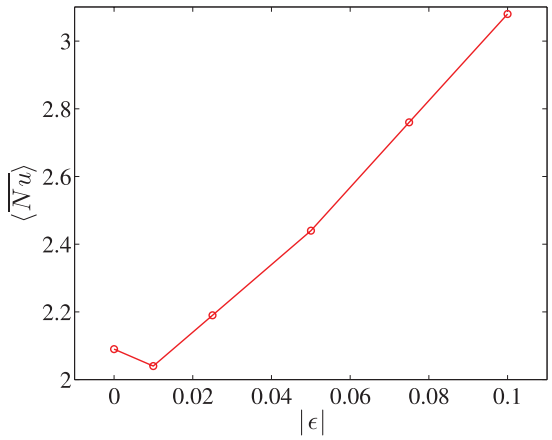

Figure 10. Time and azimuthally averaged Nusselt number, $\langle \overline{Nu} \rangle$, as a function of the absolute value of the topographic amplitude, $|\epsilon|$, for $E = 10^{-6}$ and $\widehat{Ra} = 8$.

4 DISCUSSION

We have developed a quasigeostrophic numerical model of turbulent core convection in which a single Gaussian ridge is superposed on the outer spherical surface to model the effects of cold downwelling mantle material impinging on the CMB. To simplify the problem and delineate the basic response of the system, we have not considered the effects of a magnetic field. The use of the 2-D QGCM in our study allows for the simulation of rapidly rotating, low-Prandtl number turbulent flows (i.e. low Ekman number, high Reynolds number flows) that are currently out of reach to 3-D simulations. By varying the Ekman number, the Rayleigh number and the topographic amplitude, we have highlighted the important fluid dynamical effects that topography can have in Earth's core.

The presence of the ridge results in the excitation of topographic Rossby waves, and an increase in the convective vigour as the topographic amplitude is increased. In agreement with previous work at lower Reynolds numbers (Herrmann & Busse 1998), the time-averaged flow field reveals a resonant, stationary Rossby wave that is excited in the downstream region of the topography. The presence of this wave results in the formation of recirculating regions that are fixed relative to the mantle. Associated with the stationary Rossby wave is an azimuthally varying heat flux. Differences in the Nusselt number along the inner boundary are observed to be as large as 55 per cent for the highest Rayleigh number investigated at $E = 10^{-6}$. Furthermore, we have found that the effects of topography are similar for both positive and negative topographic amplitudes; this result suggests that both ridges and valleys have roughly the same

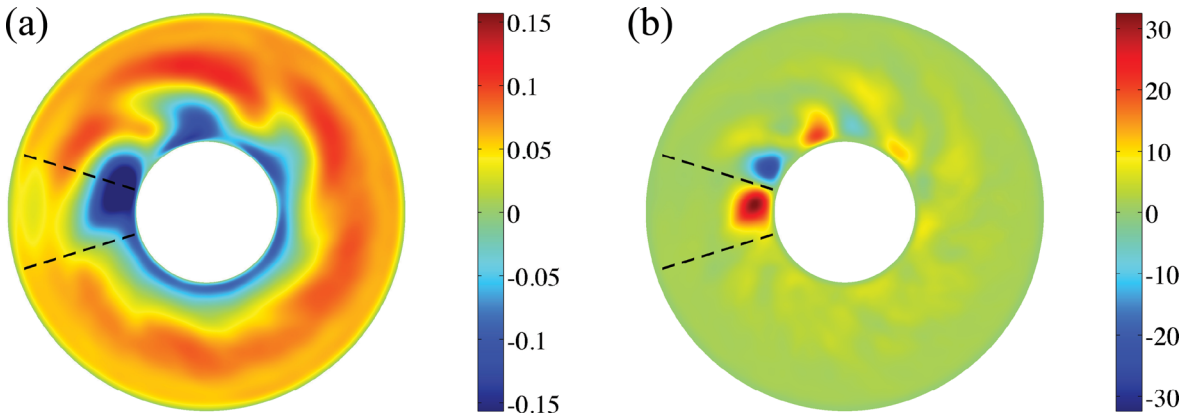

Figure 11. (a) Time-averaged temperature perturbation, $\overline{\theta}$ and (b) convective heat flux, $\overline{u'\theta'}$ for $E = 10^{-6}$, $\widehat{Ra} = 8$ and $\epsilon = -0.10$.

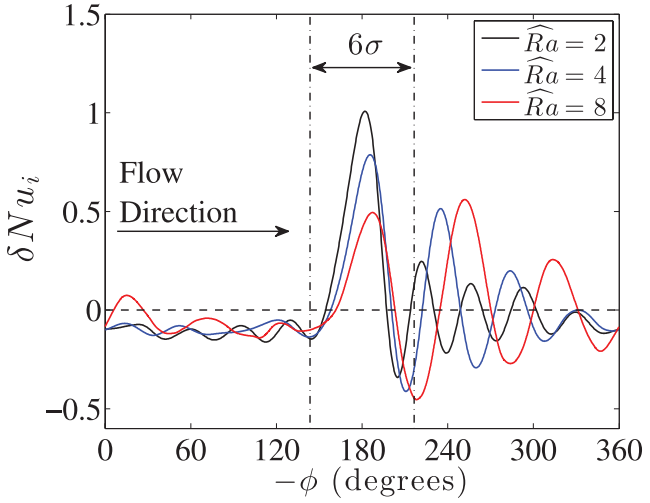

Figure 12. Azimuthal variation in time-averaged Nusselt number along the inner boundary (r_i) for $E = 10^{-6}$, $\epsilon = -0.10$ and $\widehat{Ra} = 2, 4, 8$. The vertical dot-dashed lines demarcate the region occupied by the topographic ridge of width 6σ. The zonal flow near the inner boundary travels from left to right with respect to the figure.

influence on flow behaviour in the core. Furthermore, results from a simulation employing a circular, Gaussian bump with identical σ value show the same general features as those observed for the Gaussian ridge topography employed in this study.

We find that the effects of the topography become more significant as the Ekman number is reduced. This result is expected because the presence of friction acts to reduce the amplitude of the resonant topographic Rossby wave. In this sense, the presence of the ridge (and the overall structure of the bounding surfaces) becomes less important for controlling the dynamics as the Ekman number is increased. Because the Ekman numbers employed in the current study are up to 10 orders of magnitude larger than that for the core, we consider topographic amplitudes that are up to two orders of magnitude larger than that expected for the CMB such that the primary effects are manifested. However, if one compares the $E^{1/2}$ thickness of the Ekman boundary layer on the CMB to the topographic amplitude ϵ, we have a 'scaled' topographic amplitude in the core of $\epsilon^{'} = \epsilon/E^{1/2} \sim 10^4$. For the values used in our study we have $\epsilon^{'} \approx 10 - 10^2$. A turbulent Ekman layer may reduce this ratio in the core to $\epsilon^{'}_{\rm turb} \sim 10^2$. Thus, these values suggest that the viscously scaled topographic amplitudes employed in our study may be comparable to those in the core. Based on preliminary results from simulations at lower Ekman numbers, we surmise that realistic topographic amplitudes of $\epsilon \sim 10^{-3}$ will have significant effects on the convective dynamics of our simulations if we are able to reduce the Ekman number by up to three orders of magnitude ($E \approx 10^{-9}$). This suggests that CMB topography will influence, and possibly even control, the flow field and heat transfer of the outer core.

Our study demonstrates that static features in the flow field can be produced by the interaction of turbulent convective motions with CMB topography. These steady features result from resonance between a stationary Rossby wave and the underlying topography. A simple linear analysis shows that the resonant wavenumber, L_R, scales as $L_R \sim Ro^{-1/2}$, where Ro is the Rossby number. This scaling shows that viscous effects and the precise shape of the topography do not play a significant role in determining the resonant mode. Rather, the location of the topography on the CMB will determine where the flow field is affected. More simulations are necessary to test the veracity of this $L_R \sim Ro^{-1/2}$ scaling and to determine the necessary proportionality prefactor. For instance, if we estimate the Rossby number for the core to be $Ro \sim 10^{-6}$, our scaling predicts $L_R \sim 10^3$. We find that the theoretical value is typically $\approx$5 times larger than the observed wavenumber (see Fig. 6). Applying this factor reduces the resonant wavenumber in the core down to $L_R \approx 200$. This value remains significantly larger than that which is observed in the time-averaged geomagnetic field observations, where the dominant azimuthal magnetic wavenumber is $L_{\rm mag} \approx 3-8$ (e.g. Hulot *et al.* 2002; Jackson 2003).

The core's large magnetic diffusivity may partially account for the discrepancy between the observed dominant wavenumber in the time-averaged geomagnetic field and the wavenumber predicted by linear Rossby wave resonance theory. For instance, the magnetic Prandtl number for the core is thought to be $Pm = \nu/\nu_{\rm mag} \approx 10^{-6}$, where $\nu_{\rm mag}$ is the magnetic diffusivity. This extremely small value suggests that there is a significant separation of scales between the flow field and the magnetic structures of the core; small scale flows may still be associated with large scale magnetic fields because of the importance of magnetic diffusion. Thus, we hypothesize that a high wavenumber [$\mathcal{O}(10^2 - 10^3)$], topographically excited resonant mode is characterized by a much lower wavenumber [i.e. $\lesssim \mathcal{O}(10)$] magnetic signature.

Recent work has employed the quasigeostrophic approximation to calculate the flow field in the equatorial plane of the core based on inversions of the geomagnetic field (Pais & Jault 2008; Gillet *et al.* 2009). These studies, which include no boundary topography, show a flow field that is dominated by coherent vortices and a meandering retrograde mean flow. In particular, Pais & Jault (2008) observe coherent axial vortices with an approximately equal proportion of cyclones and anticyclones. Our simulations carried out at $E = 10^{-6}$ also show an approximately equal proportion of cyclonic and anticyclonic regions, though the anticyclonic vortices are generally larger than the cyclones and exist primarily near the ICB. In addition, the topographic Rossby wave that is excited by the ridge in our simulations results in a flow pattern that bears striking similarity to the streamfunction contours found by Pais & Jault (2008) and Gillet *et al.* (2009).

Finally, our results show that topography can produce significant longitudinal variations in radial heat flux along the ICB (see Table 1 and Fig. 12). Similar results were found in the laboratory experiments of Sumita & Olson (1999, 2002), which examined the effects of a 'thermal ridge' on high Rayleigh number convection in a rapidly rotating hemispherical shell of water. Sumita & Olson (1999, 2002) argued that lateral heat flux variations along the ICB can explain the observed seismic structure of the inner core (e.g. Niu & Wen 2001). The recent work of Alboussiére *et al.* (2010) and Monnereau *et al.* (2010) further suggests that such heterogeneous thermal boundary conditions on the ICB can control the location of melting and freezing of iron. Because topography provides a mechanism to modulate the heat flux along the ICB, it is possible that CMB topography controls the growth pattern of the ICB (*cf.* Sumita & Olson 1999, 2002; Aubert *et al.* 2008; Gubbins *et al.* 2011).

We have investigated the fundamental phenomena that arise in the interaction of core-style turbulent convection with a CMB topographic feature. Future work will focus on reducing the effects of viscosity such that realistic topographic amplitudes can be used ($\epsilon \lesssim 10^{-3}$), as well as incorporating more realistic models of CMB topography (e.g. Tanaka 2010). We will also look at the effects of a magnetic field, which can change the dynamics of the resonant mode (e.g. Finlay 2007; Finlay *et al.* 2010).

ACKNOWLEDGMENTS

The authors wish to thank M. Dumberry and an anonymous referee for careful reviews that greatly improved this manuscript. MAC, JN and JMA received support for this project from NSF's Geophysics Program (awards EAR-0610093 and EAR-0944312) and NASA's PGG Program (award NNX09AE96G). MAC also gratefully acknowledges support via a NSF EAR Postdoctoral Fellowship. Computing time was provided by NAS HEC (award SMD-09-1274).

REFERENCES

Alboussiére, T., Deguen, R. & Melzani, M., 2010. Melting-induced stratification above the Earth's inner core due to convective translation, *Nature,* **466,** 744–747.

Anufriev, A.P. & Braginsky, S.I., 1975. Influence of irregularities of the boundary of the Earth's core on the velocity of the liquid and on the magnetic field, *Geomagn. & Aeron.,* **15,** 754–757.

Anufriev, A.P. & Braginsky, S.I., 1977a. Influence of irregularities of the boundary of the Earth's core on the velocity of the liquid and on the magnetic field, II, *Geomagn. Aeron.,* **17,** 78–82.

Anufriev, A.P. & Braginsky, S.I., 1977b. Influence of irregularities of the boundary of the Earth's core on the velocity of the liquid and on the magnetic field, III, *Geomagn. Aeron.,* **17,** 492–496.

Aubert, J., Brito, D., Nataf, H.-C., Cardin, P. & Masson, J.-P., 2001. A systematic experimental study of rapidly rotating spherical convection in water and liquid gallium, *Phys. Earth planet. Inter.,* **128,** 51–74.

Aubert, J., Gillet, N. & Cardin, P., 2003. Quasi-geostrophic models of convection in rotating spherical shells, *Geochem. Geophys. Geosyst.,* **4**(7), doi:10.1029/2002GC000456.

Aubert, J., Amit, H., Hulot, G. & Olson, P., 2008. Thermochemical flows couple the Earth's inner core growth to mantle heterogeneity, *Nature,* **454,** 758–762.

Aurnou, J.M. & Olson, P., 2001. Experiments on Rayleigh–Bénard convection, magnetoconvection, and rotating magnetoconvection in liquid gallium, *J. Fluid Mech.,* **430,** 283–307.

Bassom, A.P. & Soward, A.M., 1996. Localised rotating convection induced by topography, *Physica D,* **97,** 29–44.

Bell, P.I. & Soward, A.M., 1996. The influence of surface topography on rotating convection, *J. Fluid Mech.,* **313,** 147–180.

Bloxham, J. & Gubbins, D., 1987. Thermal core-mantle interactions, *Nature,* **325,** 511–513.

Brummell, N.H. & Hart, J.E., 1993. High Rayleigh number β-convection, *Geophys. Astrophys. Fluid Dyn.,* **68,** 85–114.

Busse, F.H., 1970. Thermal instabilities in rapidly rotating systems, *J. Fluid Mech.,* **44,** 441–460.

Calkins, M.A., Noir, J., Eldredge, J.D. & Aurnou, J.M., 2010. Axisymmetric simulations of libration-driven fluid dynamics in a spherical shell geometry, *Phys. Fluids,* 22, 086602, doi:10.1063/1.3475817.

Cardin, P. & Olson, P., 1994. Chaotic thermal convection in a rapidly rotating spherical shell: consequences for flow in the outer core, *Phys. Earth planet. Inter.,* **82,** 235–239.

Cardin, P. & Olson, P., 1995. The influence of toroidal magnetic field on thermal convection in the core, *Earth planet. Sci. Lett.,* **132,** 167–181.

Carlut, J. & Courtillot, V., 1998. How complex is the time-averaged geomagnetic field over the last 5 Million years? *Geophys. J. Int.,* **134,** 527–544.

Charney, J.G. & DeVore, J.G., 1979. Multiple flow equilibria in the atmosphere and blocking, *J. Atmos. Sci.,* **36,** 1205–1216.

Cioni, S., Chaumat, S. & Sommeria, J., 2000. Effect of a vertical magnetic field on turbulent Rayleigh–Bénard convection, *Phys. Rev. E,* **62**(4), doi:10.1103/PhysRevE.62.R4520.

Davies, C., Gubbins, D. & Jimack, P., 2009. Convection in a rotating spherical fluid shell with an imposed laterally varying thermal boundary condition, *J. Fluid Mech.,* **641,** 335–358.

Doornbos, D.J. & Hilton, T., 1989. Models of the core-mantle boundary and travel-times of internally reflected core phases, *J. geophys. Res.,* **94**(15), 741–751.

Finlay, C.C., 2007. Magnetohydrodynamic waves, in *Encyclopedia of Geomagnetism and Paleomagnetism,* eds Gubbins, D. & Herrero-Bervera, E., Springer, Dordrecht.

Finlay, C.C., Dumberry, M., Chulliat, A. & Pais, M.A., 2010. Short timescale core dynamics: theory and observations, *Space Sci. Rev.,* **155,** 177–218.

Gillet, N. & Jones, C.A., 2006. The Quasi-geostrophic model for rapidly rotating spherical convection outside the tangent cylinder, *J. Fluid Mech.,* **554,** 343–369.

Gillet, N., Brito, D., Jault, D. & Nataf, H.-C., 2007. Experimental and numerical studies of convection in a rapidly rotating spherical shell, *J. Fluid Mech.,* **580,** 83–121.

Gillet, N., Pais, M.A. & Jault, D., 2009. Ensemble inversion of time-dependent core flow models, *Geochem. Geophys. Geosyst.,* **10**, Q06004, doi:10.1029/2008GC002290.

Greenspan, H.P., 1968. *The Theory of Rotating Fluids,* Cambridge University Press, London.

Grooms, I., Julien, K., Weiss, J.B. & Knobloch, E., 2010. Model of convective Taylor columns in rotating Rayleigh–Bénard convection, *Phys. Rev. Lett.,* **104**, 224501, doi:10.1103/PhysRevLett.104.224501.

Gubbins, D. & Bloxham, J., 1987. Morphology of the geomagnetic field and implications for the geodynamo, *Nature,* **325,** 509–511.

Gubbins, D. & Kelly, P., 1993. Persistent patterns in the geomagnetic field over the past 2.5 Myr, *Nature,* **365,** 829–832.

Gubbins, D., Sreenivasan, B., Mound, J. & Rost, S., 2011. Melting of the Earth's inner core, *Nature,* **473,** 361–263.

Held, I.M., Ting, M. & Wang, H., 2002. Northern winter stationary waves: theory and modeling, *J. Climate,* **15,** 2125–2144.

Herrmann, J. & Busse, F.H., 1998. Stationary and time dependent convection in the rotating cylindrical annulus with modulated height, *Phys. Fluids,* **10**(7), 1611–1620.

Hide, R., 1969. Interaction between the Earth's liquid core and solid mantle, *Nature,* **222,** 1055–1056.

Hide, R., Boggs, D.H., Dickey, J.O., Dong, D., Gross, R.S. & Jackson, A., 1996. Topographic core-mantle coupling and polar motions on decadal time-scales, *Geophys. J. Int.,* **125,** 599–607.

Hulot, G., Huy, M.L. & Mouël, J.L.L., 1996. Influence of core flows on the decade variations of the polar motion, *Geophys. Astrophys. Fluid Dyn.,* **82,** 35–67.

Hulot, G., Eymin, C., Langlais, B., Mandea, M. & Olsen, N., 2002. Small-scale structure of the geodynamo inferred from Oersted and Magsat satellite data, *Nature,* **416,** 620–623.

Jackson, A., 2003. Intense equatorial flux spots on the surface of the earth's core, *Nature,* **424,** 760–763.

Jault, D. & Le Mouël, J.-L., 1989. The topographic torque associated with a tangentially geostrophic motion at the core surface and inferences on the flow inside the core, *Geophys. Astrophys. Fluid Dyn.,* **48,** 273–296.

Jault, D. & Le Mouël, J.-L., 1990. Core-mantle boundary shape: constraints inferred from the pressure torque acting between the core and the mantle, *Geophys. J. Int.,* **101,** 233–241.

Jault, D. & Le Mouël, J.-L., 1991. Exchange of angular momentum between the core and the mantle, *J. Geomag. Geoelectr.,* **43,** 111–129.

Johnson, C. & Constable, C., 1997. The time-averaged geomagnetic field: global and regional biases for 0-5 Ma, *Geophys. J. Int.,* **131,** 643–666.

Jones, C.A., Rotvig, J. & Abdulrahman, A., 2003. Multiple jets and zonal flow on Jupiter, *Geophys. Res. Lett.,* **30**(14), doi:10.1029/2003GL016980.

Kelly, P. & Gubbins, D., 1997. The geomagnetic field over the past 5 Myr, *Geophys. J. Int.,* **128,** 315–330.

King, E.M., Stellmach, S., Noir, J., Hansen, U. & Aurnou, J.M., 2009. Boundary layer control of rotating convection systems, *Nature,* **457,** 301–304.

King, E.M., Soderlund, K.M., Christensen, U.R., Wicht, J. & Aurnou, J.M., 2010. Convective heat transfer in planetary dynamo models, *Geochem. Geophys. Geosyst.,* **11**(6), doi:10.1029/2010GC003053.

Korte, M. & Constable, C., 2006. Centennial to millennial geomagnetic secular variation, *Geophys. J. Int.,* **167,** 43–52.

Kuang, W.-J. & Bloxham, J., 1993. The effect of boundary topography on motions in the Earth's core, *Geophys. Astrophys. Fluid Dyn.,* **72,** 161–195.

Kuang, W.-J. & Chao, B.F., 2001. Topographic core-mantle coupling in geodynamo modeling, *Geophys. Res. Lett.,* **28**(9), 1871–1874.

Lassak, T.-M., McNamara, A.K. & Zhong, S., 2007. Influence of thermo-chemical piles on topography at Earth's core-mantle boundary, *Earth planet. Sci. Lett.,* **261,** 443–455.

Lassak, T.-M., McNamara, A.K., Garnero, E.J. & Zhong, S., 2010. Core-mantle boundary topography as a possible constraint on lower mantle chemistry and dynamics, *Earth planet. Sci. Lett.,* **289,** 232–241.

Legras, B. & Ghil, M., 1985. Persistent anomalies, blocking and variations in atmospheric predictability, *J. Atmos. Sci.,* **42**(5), 433–471.

Maxworthy, T., 1977. Topographic effects in rapidly-rotating fluids: flow over a transverse ridge, *J. appl. Math. Phys. (ZAMP),* **28,** 853–864.

Moffatt, H., 1978. Topographic coupling at the core-mantle interface, *Geophys. Astrophys. Fluid Dyn.,* **9,** 279–288.

Monnereau, M., Calvet, M., Margerin, L. & Souriau, A., 2010. Lopsided growth of Earth's inner core, *Science,* **328,** 1014–1017.

Morelli, A. & Dziewonski, A.M., 1987. Topography of the core-mantle boundary and lateral homogeneity of the liquid core, *Nature,* **325,** 678–683.

Morin, V. & Dormy, E., 2004. Time dependent β-convection in rapidly rotating spherical shells, *Phys. Fluids,* **16**(5), 1603–1609.

Morin, V. & Dormy, E., 2006. Dissipation mechanisms for convection in rapidly rotating spheres and the formation of banded structures, *Phys. Fluids,* **18**, 068104, doi:10.1063/1.2215605.

Niu, F.L. & Wen, L.X., 2001. Hemispherical variations in seismic velocity at the top of the Earth's inner core, *Nature,* **410,** 1081–1084.

Pais, M.A. & Jault, D., 2008. Quasi-geostrophic flows responsible for the secular variation of the Earth's magnetic field, *Geophys. J. Int.,* **173,** 421–443.

Pedlosky, J., 1987. *Geophysical Fluid Dynamics,* Springer-Verlag, New York, NY.

Peyret, R., 2002. *Spectral Methods for Incompressible Viscous Flow,* Vol. 148. Springer-Verlag, New York, NY.

Pfeffer, R.L., Kung, R., Ding, W. & Li, G.-Q., 1993. Barotropic flow over bottom topography—experiments and nonlinear theory, *Dyn. Atmos. Oceans,* **19,** 101–114.

Read, P.L. & Risch, S.H., 2011. A laboratory study of global-scale wave interactions in baroclinic flow with topography i: multiple flow regimes, *Geophys. Astrophys. Fluid Dyn.,* **105,** 128–160.

Rodgers, A. & Wahr, J., 1993. Inference of core-mantle boundary topography from ISC, PcP and PKP traveltimes, *Geophys. J. Int.,* **115,** 991–1011.

Schaeffer, N. & Cardin, P., 2005. Quasi-geostrophic model of the instabilities of the Stewartson layer in flat and depth-varying containers, *Phys. Fluids,* **17**, 104111, doi:10.1016/j.epsl.2006.03.024.

Schaeffer, N. & Cardin, P., 2006. Quasi-geostrophic kinematic dynamos at low magnetic Prandtl number, *Earth planet. Sci. Lett.,* **245,** 595–604.

Schaeffer, N. & Pais, M.A., 2011. On symmetry and anisotropy of Earth-core flows, *Geophys. Res. Lett.,* **38**, L10309, doi:10.1029/2011GL046888.

Sprague, M., Julien, K., Knobloch, E. & Werne, J., 2006. Numerical simulation of an asymptotically reduced system for rotationally constrained convection, *J. Fluid Mech.,* **551,** 141–174.

Sumita, I. & Olson, P., 1999. Convection in Earth's core driven by a thermally heterogeneous mantle, *Science,* **286,** 1547–1549.

Sumita, I. & Olson, P., 2002. Rotating thermal convection experiments in a hemispherical shell with hetergeneous boundary heat flux: implications for the Earth's core, *J. geophys. Res.,* **107**(B8), doi:10.1029/2001JB000548.

Sze, E.K.M. & van der Hilst, R.D., 2003. Core-mantle boundary topography from short period PcP, PKP, and PKKP data, *Phys. Earth planet. Inter.,* **135,** 27–46.

Takehiro, S. I., 2008. Physical interpretation of spiralling-columnar convection in a rapidly rotating annulus with radial propagation properties of Rossby waves, *J. Fluid Mech.,* **614,** 67–86.

Tanaka, S., 2010. Constraints on the core-mantle boundary topography from P4KP-PcP differential travel times, *J. geophys. Res.,* **115**, B04310, doi:10.1029/2009JB006563.

Tian, Y., Weeks, E.R., Ide, K., Urbach, J.S., Baroud, C.N., Ghil, M. & Swinney, H.L., 2001. Experimental and numerical studies of an eastward jet over topography, *J. Fluid Mech.,* **438,** 129–157.

Tritton, D.J., 2001. *Physical Fluid Dynamics,* Oxford University Press, New York, NY.

Vallis, G.K., 2006. *Atmospheric and Oceanic Fluid Dynamics,* Cambridge University Press, Cambridge.

Weeks, E.R., Tian, Y., Urbach, J.S., Ide, K., Swinney, H. & Ghil, M., 1997. Transitions between blocked and zonal flows in a rotating annulus with topography, *Science,* **278,** 1598–1601.

Westerburg, M. & Busse, F.H., 2003. Centrifugally driven convection in the rotating cylindrical annulus with modulated boundaries, *Nonlinear Proc. Geophys.,* **10,** 275–280.

Willis, A.P., Sreenivasan, B. & Gubbins, D., 2007. Thermal core-mantle interaction: exploring regimes for 'locked' dynamo action, *Phys. Earth planet. Inter.,* **165,** 83–92.

Wolff, J.-O., Maier-Reimer, E. & Olbers, D.J., 1991. Wind-driven flow over topography in a zonal β-plane channel: a Quasi-geostrophic model of the antarctic circumpolar current, *J. Phys. Ocean.,* **21,** 236–263.

Yanagisawa, T., Yamagishi, Y., Hamano, Y., Tasaka, Y., Yoshida, M., Yano, K. & Takeda, Y., 2010. Structure of large-scale flows and their oscillation in the thermal convection of liquid gallium, *Phys. Rev. E,* **82**, 016320, doi:10.1103/PhysRevE.82.016320.

Yano, J. I., Talagrand, O. & Drossart, P., 2005. Deep two-dimensional turbulence: an idealized model for atmospheric jets of the giant outer planets, *Geophys. Astrophys. Fluid Dyn.,* **99**(2), 137–150.

Yoshida, M., 2008. Core-mantle boundary topography estimated from numerical simulations of instantaneous mantle flow, *Geochem. Geophys. Geosyst.,* **9**, Q07002, doi:10.1029/2008GC002008.

Zhang, K.K. & Gubbins, D., 1993. Convection in a rotating spherical fluid shell with inhomogeneous temperature boundary condition at infinite Prandtl number, *J. Fluid Mech.,* **250,** 209–232.

SUPPORTING INFORMATION

Additional Supporting Information may be found in the online version of this article:

Movie 1. Movie showing axial vorticity at $E = 10^{-5}$, $\widehat{Ra} = 8$, $\epsilon = 0$. Time is given in units of dimensionless rotation time, $t_\Omega = t_\kappa Pr/(2\pi E)$, where t_κ is the dimensionless thermal diffusion-scaled time. Red is positive (cyclonic) vorticity and blue is negative (anticyclonic) vorticity.

Movie 2. Movie showing axial vorticity at $E = 10^{-5}$, $\widehat{Ra} = 8$, $\epsilon = -0.10$. Time and vorticity are defined as in Movie 1.

Movie 3. Movie showing axial vorticity at $E = 10^{-6}$, $\widehat{Ra} = 8$, $\epsilon = 0$. Time and vorticity are defined as in Movie 1.

Movie 4. Movie showing axial vorticity at $E = 10^{-6}$, $\widehat{Ra} = 8$, $\epsilon = -0.10$. Time and vorticity are defined as in Movie 1.

Movie 5. Movie showing axial vorticity at $E = 10^{-6}$, $\widehat{Ra} = 8$, $\epsilon = -0.10$ in the vicinity of the topographic ridge. Time and vorticity are defined as in Movie 1.

Please note: Wiley-Blackwell are not responsible for the content or functionality of any supporting materials supplied by the authors. Any queries (other than missing material) should be directed to the corresponding author for the article.